IEEE ComSoc IEEE Communications Society | IEEE COMPUTER SOCIETY | IEEE Signal Processing Society | VTS Connecting the Mobile World | IEEE Transactions on Machine Learning in Communications and Networking

Received 15 January 2024; revised 17 May 2024 and 20 June 2024; accepted 22 June 2024.
Date of publication 25 June 2024; date of current version 2 July 2024.

The associate editor coordinating the review of this article and approving it for publication was M. Mozaffari.

Digital Object Identifier 10.1109/TMLCN.2024.3418933

GenAI-Based Models for NGSO Satellites Interference Detection

ALMOATSSIMBILLAH SAIFALDAWLA (Graduate Student Member, IEEE), FLOR ORTIZ (Member, IEEE), EVA LAGUNAS (Senior Member, IEEE), ABUZAR B. M. ADAM (Member, IEEE), AND SYMEON CHATZINOTAS (Fellow, IEEE)

Interdisciplinary Centre for Security Reliability and Trust (SnT), University of Luxembourg, 1855 Kirchberg, Luxembourg
CORRESPONDING AUTHOR: A. SAIFALDAWLA (moatssim.saifaldawla@uni.lu)

This work was supported by Luxembourg National Research Fund (FNR) under the Project SmartSpace under Grant C21/IS/16193290.

ABSTRACT Recent advancements in satellite communications have highlighted the challenge of interference detection, especially with the new generation of non-geostationary orbit satellites (NGSOs) that share the same frequency bands as legacy geostationary orbit satellites (GSOs). Despite existing radio regulations during the filing stage, this heightened congestion in the spectrum is likely to lead to instances of interference during real-time operations. This paper addresses the NGSO-to-GSO interference problem by proposing advanced artificial intelligence (AI) models to detect interference events. In particular, we focus on the downlink interference case, where signals from low-Earth orbit satellites (LEOs) potentially impact the signals received at the GSO ground stations (GGSs). In addition to the widely used autoencoder-based models (AEs), we design, develop, and train two generative AI-based models (GenAI), which are a variational autoencoder (VAE) and a transformer-based interference detector (TrID). These models generate samples of the expected GSO signal, whose error with respect to the input signal is used to flag interference. Actual satellite positions, trajectories, and realistic system parameters are used to emulate the interference scenarios and validate the proposed models. Numerical evaluation reveals that the models exhibit higher accuracy for detecting interference in the time-domain signal representations compared to the frequency-domain representations. Furthermore, the results demonstrate that TrID significantly outperforms the other models as well as the traditional energy detector (ED) approach, showing an increase of up to 31.23% in interference detection accuracy, offering an innovative and efficient solution to a pressing challenge in satellite communications.

INDEX TERMS Non-geostationary orbit satellites (NGSOs), geostationary orbit satellites (GSOs), interference detection, satellite communication, generative AI (GenAI).

I. INTRODUCTION

A. CONTEXT AND MOTIVATION

AMONG the dynamic field of satellite communications, the co-existence between non-geostationary (NGSO) and geostationary (GSO) satellite systems has become an increasingly important issue, due to the increasing number of satellites in NGSO, particularly in low-Earth orbit (LEO) [1]. This co-existence may lead to the possibility that NGSO satellites inadvertently degrade GSO communication with GSO ground stations (GGSs), which can severely impair the quality and reliability of vital communication services for many global applications [2]. To address this problem, the International Telecommunication Union (ITU) mandates a power radiation checkpoint whenever an NGSO operator files for a specific spectrum use, this is often referred to as the equivalent-power flux density (EPFD) limits [3]. This checkpoint is found to be too relaxed for GSO operators and too strict for NGSO operators [4]. Tackling interference effectively requires a multifaceted approach, encompassing several stages: monitoring of interference [5], [6], detection of interference [7], classification of interference types [8], pinpointing the location of interference [9], and finally, mitigating interference [2], [10]. In our paper, we focus on the aspect of interference detection problem. Traditional interference detection methods, such as energy detectors (EDs), are increasingly inadequate in this evolving landscape [11].

EDs primarily measure the energy of a signal to determine the presence of an interference signal by thresholding over signal power. However, in a densely populated orbital environment, where there are many low-power signals, EDs may not have the sensitivity to detect weak or hidden interfering signals in the background noise. This lack of sensitivity can lead to missed detections.

The limitations of traditional interference detection techniques set the stage for exploring advanced machine learning (ML) techniques as possible solutions [12]. Consequently, various advents in generative artificial intelligence (GenAI), in which advanced algorithms are trained to create new original content [13], such as variational autoencoder models (VAEs) [14] and recent transformer-based models [15], could offer a new paradigm for complex interference detection tasks. Our research focuses on highlighting the promising benefits of GenAI in interference detection tasks for satellite communication systems. These benefits include improved accuracy, adaptability, and predictive capability, which help overcome the limitations of conventional methods.

B. RELATED WORK

1) INTERFERENCE DETECTION BASED ON TRADITIONAL TECHNIQUES

The current state of the art in interference detection within satellite communications predominantly revolves around traditional techniques that have been instrumental in interference detection problems [16].

The optimal detector depends on the amount of side-information that we have with respect to the signal to be detected. Since we generally do not have much information, the optimal detector (also known as the likelihood-ratio test) for stochastic signals in white Gaussian noise environments is the ED [16]. An ED essentially measures the energy of the received signals and compares it to a specific threshold, which makes a binary decision on the presence of interference. The simplicity and low computational requirements of EDs make them popular in scenarios where fast and direct detection is needed [11]. However, they have limitations in environments with complex signal characteristics or low signal-to-noise ratios (SNRs) [17]. In these cases, energy detectors can face difficulties in distinguishing between legitimate signals and interference, resulting in false positives or missed detections. Among the challenges of ED, the most relevant is the definition of the time window where the energy is calculated, as well as the establishment of an appropriate threshold [18].

Regarding the use of ED in space-based applications, Politis et al. [7] presented a novel two-step algorithm to detect interference in satellite communications using on-board spectrum monitoring units (SMUs). Focusing on the use of the DVB-S2X standard [7], [19] leverages pilot symbols for data transmission. The proposed method involves removing pilot signals from the received signal and applying an ED technique, showing superior performance to conventional ED, especially in low interference-to-signal and noise ratios (ISNRs). A significant limitation of this methodology is that the complexity and power consumption of on-board processing need to be optimized, as these are critical factors for in-orbit systems.

Another popular technique is the detection of cyclostatinarity. For instance, Dimc et al. [20] examined cyclostationary feature detection for mobile satellite transmission. Although this technique overcomes the limitations of ED in low-SNR environments, it requires high computational complexity since all the cycle frequencies need to be calculated. Such complexity poses challenges in fast time-varying scenarios such as those included in this work, where the NGSO satellite(s) quick propagation results in a relatively short-time interference impact on the desired signal.

In general, key challenges faced by traditional techniques include their limited adaptability to rapidly changing and increasingly crowded satellite environments, the requirement for more sophisticated real-time processing and analysis capabilities, and dependence on external factors such as signal strength and environmental conditions. These challenges highlight the need for more advanced, flexible, and robust interference detection methodologies as the satellite communications landscape evolves.

2) MACHINE LEARNING FOR INTERFERENCE DETECTION

ML in satellite communication operations, particularly for interference detection, has seen remarkable advances in recent years. Machine learning models offer several advantages over traditional methods, such as improved accuracy, adaptability to complex signal environments, and the ability to learn and predict interference patterns [21], [22]. However, the integration of ML models into existing systems and the trade-off between computational efficiency and detection performance remain areas of ongoing research and development [23].

In this context, Pellaco et al. [24], presented an autoencoder-based long-short term memory model (LSTM), or LSTMAE, to identify both short-term and long-term interference within the spectrum of NGSO satellite signals at GSO ground stations, the goal was to detect deliberate interference or jamming, which was artificially created and added to the NGSO communication signal. Vazquez et al. [12], utilized a convolutional autoencoder (CAE) model to classify signals by processing in-phase and quadrature (IQ) samples directly. The primary signal considered is from a GSO satellite link, while interference is presumed to come from ground-based cellular networks. Saifaldawla et al. [25], proposed a conventional autoencoder model (AE) to detect interference from NGSO system to a GSO ground station in time and frequency domains data representations. The authors investigate the scenario of single NGSO satellite, and single modulation schemes (ModCods) for both GSO and NGSO.

The aforementioned investigations [12], [24], [25] are limited to only high-level and simplified scenarios. Consequently, significant challenges remain in the application of ML for interference detection in satellite communication. In this paper, we investigate the use of VAE and a transformer-based interference detector (TrID) models' capabilities for interference detection tasks in satellite communications, and we also address some of the existing interference detection challenges, which include the need for large and diverse datasets for training, the complexity of real-time processing, and adapting approaches to the dynamic nature of satellite communication environments. To the best of our knowledge, this is the first paper to investigate the use of VAE and TrID for interference detection tasks in satellite communications.

C. CONTRIBUTIONS

The key contributions of this paper to the field of satellite communication, particularly in the area of interference detection between NGSOs and GSO satellite systems, can be stated as follows,

- The main contribution of this work is to design, develop, and investigate GenAI-based models (i.e., VAE and TrID models) capabilities for NGSOs-to-GSO interference detection tasks in satellite communications.
- We present a detailed evaluation of the proposed GenAI-based models against benchmark ML models, that is, AE, CAE, and LSTMAE, to detect interference instances in both time-domain and frequency-domain representations of the GGS received signal. This evaluation is one of the first to assess GenAI-based models in the context of satellite interference detection.
- We then provide a comparative analysis between the proposed GenAI-based models and a traditional detection methods, such as EDs, within the same NGSO interference conditions, to critically analyze their performance. This comparison highlights the strengths and limitations of both traditional and modern GenAI-based approaches in various satellite interference scenarios.
- Within this analysis, we explored the impact of varying GSO modulation schemes and bandwidth overlap scenarios on interference detection accuracy, along with the LEO off-axis arrival angles and various interference power levels.
- We implement innovative and extensive simulation and data generation methodologies to facilitate and introduce new datasets for future investigation of NGSOs-GSO interference management techniques. In which we found that the proposed GenAI-based models reconstructing ability, especially TrID, can be used to generate new interference-free data samples to train future unsupervised learning models.
- The findings reveal that the proposed models exhibit higher accuracy in detecting interference in the time-domain signal representations compared to the frequency-domain representations. Moreover, our findings demonstrate the superior detection capabilities of GenAI-based models, with TrID outstanding from the VAE and other benchmark models over the ED approach. This highlights the potential of advanced GenAI-based techniques in improving the reliability and efficiency of satellite communication systems.
- We believe that this study lays the foundation for future research in this domain. The introduced datasts, the comparative analysis, and findings offer a baseline for further exploration and enhancement of ML models in the context of increasingly complex interference-limited satellite communication systems.

D. ORGANIZATION

The remaining structure of the paper is as follows: Section II. outlines the system model, focusing on the calculation of the link budget and the model for the received digital baseband signal. Section III. discusses the simulation of NGSO-to-GSO interference scenarios and the generation of training data. Section IV. details the proposed GenAI-based models and the improved AEs models. Section V. analysis the results obtained from training the models as well as the interference detection performance. Section VII. provide a comprehensive comparison of GenAI-based models and a traditional ED approach. The paper concludes with Section VII., which provides a summary and concluding remarks.

II. SYSTEM MODEL

This research investigates the downlink dynamics of forward links originating from two distinct satellite constellations. Our main focus is on satellites in GSO orbits, as a primary system. We consider satellites in NGSO orbits, particularly those in LEO orbits, as potential sources of interference to a GGS.[1] In this section, a comprehensive description of the system model is presented, which includes aspects of link budget calculations and modeling of the received digital baseband signal.

A. LINK BUDGET MODEL

In this context, we consider that both the GSO and LEO satellites are actively transmitting signals, with the primary lobe of the transmission consistently directed toward a GGS, as shown in Fig. 1. At the GGS receiver, the carrier power received, denoted as C, from the desired GSO satellite system, can be expressed as follows

$$C = \frac{EIRP_{\text{gso}} G_{r,\text{gso}}(\theta_0)}{L_{\text{FS, gso}} L_{\text{AD}}}, \tag{1}$$

where $EIRP_{\text{gso}}$ is GSO satellite equivalent isotropic radiated power (EIRP), which quantifies the combination of the satellite antenna transmission power and its gain, $G_{r,\text{gso}}$ represents GGS maximum receiving antenna gain, θ_0 indicates the boresight angle, defining the alignment between the main lobe

[1] A general GSO ground station is assumed in the system model, which can represent either a gateway, a teleport or a user-terminal.

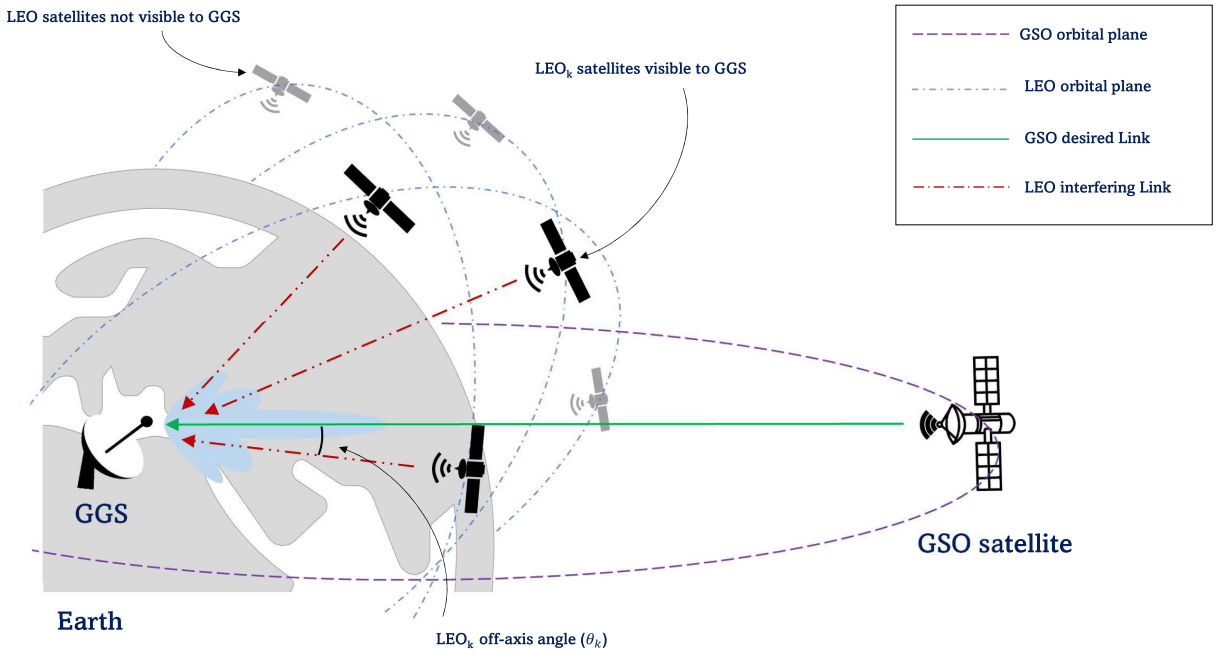

FIGURE 1. Simplified scenario scheme with a GGS pointing towards the desired GSO satellite and a potential interference from a NGSO system.

axis of GGS and GSO communication link, $L_{\text{FS, gso}}$ is the free space path loss (FSPL) at the GSO-GGS communication link with distance d_{gso}, signal wavelength λ_{gso} and carrier frequency $f_{c,\text{gso}}$. Lastly, L_{AD} correspond to the additional losses of the link (which include atmospheric, environmental, and external losses). With GGS being stationary on Earth, it consistently points towards its associated GSO satellite, which ensures optimal gain from its receiving antenna, As such, the value of (θ_0) is set to zero.

As LEO satellites traverse GGS visible sky, GGS may concurrently receive signals from one or more LEO satellites when they operate in the same frequency bands. These LEO signals primarily elevate the interference level within the primary signal. Consequently, the interference power I_k that GGS receives from an individual LEO satellite indexed as k is as follows

$$I_k = \frac{EIRP_k G_{r,k}(\theta_k) B_{\text{adj},k}}{L_{\text{FS},k} L_{\text{AD}}}, \quad k \in [1, \mathcal{K}] \tag{2}$$

where $\mathcal{K}$ represents the cumulative number of visible LEO satellites that can potentially affect the GGS at a particular time of day (time instant). $EIRP_k$ refers to the EIRP of k^{th} LEO satellite, $G_{r,k}$ denotes the GGS receiving antenna gain to k^{th} LEO satellite. Unlike (1), here θ_k represents the off-axis angle that aligns GGS beam primary lobe axis with the k^{th} LEO communication link as depicted in Fig. 1. The adjustment factor for bandwidth overlap, denoted as $B_{\text{adj},k} \in \mathbb{R}$, $B_{\text{adj},k} \in [0, 1]$, is constrained within the range [0,1], and it count for GSO and LEO bandwidth overlap, and can be calculated from the following formula

$$B_{\text{adj},k} = \frac{B_{\text{overlap},k}}{B_{i,k}}, \tag{3}$$

where $B_{\text{overlap},k}$ denotes the bandwidth overlap between the k^{th} LEO satellite bandwidth and GSO bandwidth, and $B_{i,k}$ is the bandwidth of the k^{th} LEO satellite. The value of $B_{\text{adj},k}$ adjusts the value of I_k according to the calculated ratio. Note that a full overlap of GSO and LEO bandwidths corresponds to a factor $B_{\text{adj},k} = 1$. $L_{\text{FS},k}$ convey the FSPL for the k^{th} LEO-GGS link. It should be noted that we have assumed a standardized value L_{AD} for both GSO and LEO connections, since they transmit under similar channel conditions. FSPL of the k^{th} LEO-GGS communication link with distance d_k, signal wavelength of λ_k and carrier frequency $f_{c,k}$.

The determination of the off-axis angle between GGS and the direction of the LEO satellite beam is based on the law of cosine. This relationship is expressed by the following formula

$$\theta_k = \arccos\left(\frac{d_{\text{gso}}^2 + d_k^2 - d_{\text{gso},k}}{2 d_{\text{gso}} d_k}\right), \tag{4}$$

where $d_{\text{gso},k}$ is represents the slant range between the GSO and the k^{th} LEO satellite.

In a context where transmission gain from both the GSO and LEO satellites is always at maximum, the impact of the receive antenna gain plays a pivotal role. Owing to the LEO satellite dynamic position, this receiving gain is subject to change and is influenced by the off-axis angle of the LEO satellite as observed from GGS. To make things more straightforward, we use a standard radiation pattern

to determine the receiving gain of a generic ground station receiver equipped with a parabolic antenna [26]. This gain is associated with the first-order Bessel function $\mathcal{J}_1$ [27] and can be expressed as

$$G_{r,k}(\theta_k) = G_{r,\text{gso}}(\theta_0)\left[\frac{2\lambda_k}{\pi D_A}\frac{\mathcal{J}_1\left[(\pi D_A/\lambda_k)sin(\theta_k)\right]}{sin(\theta_k)}\right], \quad (5)$$

where D_A refers to GGS antenna aperture diameter. The GGS boresight receiving gain $G_{r,\text{gso}}(\theta_0)$ is given by

$$G_{r,\text{gso}}(\theta_0) = e_A\left[\frac{\pi D_A}{\lambda_{\text{gso}}}\right]^2, \quad (6)$$

where e_A indicates the efficiency of the receiver aperture. The downlink carrier-to-noise ratio (CNR) of the GSO satellite signal received by GGS can be calculated as

$$\text{CNR} = \frac{C}{\kappa_{\text{blz}} T_{\text{temp}} B_{\text{x}}}, \quad (7)$$

where κ_{blz} represents the Boltzmann constant (1.380649×10^{-23} J/K), T_{temp} stands for the receiver noise temperature, and B_{x} is the bandwidth of the GSO baseband signal.

For interference coming from the LEO satellite, the Interference-to-Noise Ratio (INR_k) received by GGS from an individual LEO satellite indexed as k is given as

$$\text{INR}_k = \frac{I_k}{\kappa_{\text{blz}} T_{\text{temp}} B_{\text{x}}}. \quad (8)$$

Furthermore, to gauge the effect of interference imparted by all LEO satellites on the GSO system, we employ the carrier-to-interference plus noise natio (CINR) as an evaluation metric. It can be calculated as

$$\text{CINR} = \frac{C}{\sum_{k=1}^{\mathcal{K}} I_k + \kappa_{\text{blz}} T_{\text{temp}} B_{\text{x}}}. \quad (9)$$

In this context, we adopt the maximum bit error rate (BER) metric denoted by e_r and the corresponding minimum CINR denoted by CINR_{min} that must be satisfied to meet the quality of service (QoS) of the desired signal [28]. For ease of exposition, despite the different possible modulation schemes, we show hereafter an example assuming that the modulation alphabet used by both the desired and interference signals is quadrature phase-shift keying (QPSK). The corresponding CINR_{min} for QPSK is given as

$$\text{CINR}_{\text{min}} = \frac{\left[Q_{fun}^{-1}(e_r)\right]^2}{2} = \frac{\text{CNR}}{\text{INR}_{\text{max}} + 1}, \quad (10)$$

where $Q_{fun}^{-1}(\cdot)$ is the inverse Q_{fun} function. The maximum allowed interference from LEOs at GGS receiver is denoted by INR_{max} and can be found from (10) as

$$\text{INR}_{\text{max}} = \max\left(\frac{\text{CNR}}{\text{CINR}_{\text{min}}} - 1, 0\right). \quad (11)$$

B. DETAILED RECEIVED SIGNAL MODEL

In the forward link of the GSO system transmits the baseband signal $x(t)$,[2] which we will refer to as the desired transmitted signal. It can be expressed as

$$x(t) = \sum_{v=0}^{V_x-1} x[v] p_{RC_x}(t - vT_x), \quad t \in [0, V_x T_x] \quad (12)$$

where $x[v], v = 0, 1, \ldots, V_x - 1$ are modulated symbols sourced from a ModCod scheme in accordance with the DVB-S2X standard [19]. Each symbol holds an average power of P_x and lasts for a duration of T_x. The relationship between T_x and the baseband signal bandwidth B_x is given by $T_x = \frac{1}{B_x}$. Furthermore, V_x denotes the total number of symbols present in the desired signal. The function p_{RC_x} corresponds to a raised cosine filter with unit energy and duration T_x, and is incorporated with a roll-off factor between [0, 1] indicating how much power p_{RC_x} emits above a given bandwidth.

Simultaneously, one or several LEO satellites might transmit interfering signals towards the GGS. These signals can potentially cause interference with $x(t)$ in GGS. Consequently, the transmitted baseband signal $i_k(t)$ originating from the individual LEO satellite indexed as k to GGS can be expressed as

$$i_k(t) = \sum_{v=0}^{V_i-1} i_k[v] p_{RC_i}(t - vT_{i,k}), \quad t \in [0, V_i T_{i,k}] \quad (13)$$

where $i_k[v], v = 0, 1, , \ldots, V_i - 1$ are modulated symbols drawn from a ModCod scheme in accordance with the DVB-S2X standard. Each symbol holds an average power of $P_{i,k}$ and lasts for a duration of $T_{i,k}$. This duration $T_{i,k}$ correlates with the baseband signal bandwidth $B_{i,k}$ from the k^{th} LEO satellite, such that $T_{i,k} = \frac{1}{B_{i,k}}$. The function p_{RC_i} is indicative of a raised cosine filter with unit energy and duration $T_{i,k}$, and has a roll-off factor. For simplicity, we assume that $V_i T_{i,k} = V_x T_x$, that is, both the desired and interference signals blocks have the same total time duration.

In a time instant, the two signals components received by GGS are

$$y_x(t) = x(t)\sqrt{\text{CNR}} + \zeta(t), \quad (14a)$$

$$y_i(t) = \sum_{k=1}^{\mathcal{K}_t} \left(i_k(t) e^{j2\pi(f_{c,k} - f_{c,\text{gso}})t} \sqrt{\text{INR}_k}\right), \quad (14b)$$

Equation (14a) presents the desired signal components of GSO, where CNR as defined in (7), denotes the SNR of the GSO signal, and $\zeta(t)$ represents the complex-valued additive white Gaussian noise (AWGN) process, which has zero mean and maintains unity power throughout the bandwidth $2B_x$.

Equation (14b) showing the components of the interference signals, where INR_k denotes the SNR of the k^{th} LEO signal. This equation aggregates the received interfering baseband signals at GGS originating from all visible LEO satellites at a time instant. In particular, the $i_k(t)$ signal is down-converted from its bandpass form using $f_{c,\text{gso}}$. Fig. 2 shows the overlapped bandwidth ($B_{\text{overlap},k}$) between GSO and LEO.

The complex-valued time domain received signal $y(t)$ at the GGS, which encompasses the desired signal, interference

[2]Up and down conversion impairments are considered ideally compensated through standard methods.

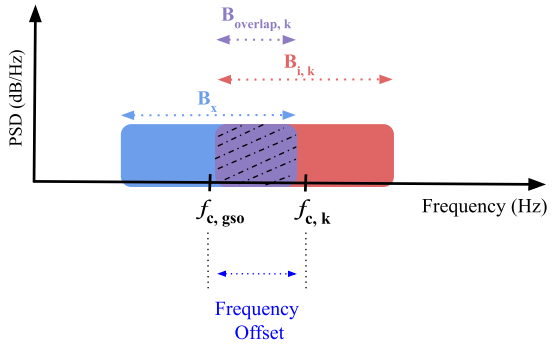

FIGURE 2. **Overlap of GSO and LEO bandwidths in frequency domain.**

Algorithm 1 Computation of CNR and INR

Input: Link Budget Parameters
Output: V_{CNR}, $\mathcal{V}_{\text{INR}}$
Initalize: V_{CNR} as a vector, $\mathcal{V}_{\text{INR}}$ as cell array
Create a satellite scenario object of period $\mathcal{T}$
Determine $\Delta(\tau)$ and N
Add GSO to the scenario using the TLE information.
Add all LEOs to the scenario using TLEs information
for $n \leftarrow 1$**to**N **do**
  Get GSO coordinations at n
  Calculate CNR_n from (7)
  Concatenate CNR_n to V_{CNR}
  Get $\mathcal{K}_n$, the number of LEOs that impact the GSO communication with GGS at n
  Initalize: $v_{\text{INR,n}}$ as an empty vector
  for $k \leftarrow 1$**to**$\mathcal{K}_n$ **do**
    Get the k^{th} LEO coordinations
    Calculate θ_k from (4)
    Calculate $G_{r,k}$ from (5)
    Calculate INR_k from (8)
    Concatenate INR_k to $v_{\text{INR,n}}$
  Compute $\text{INR}_{\text{sum,n}} = \sum_{k=1}^{\mathcal{K}_n} \text{v}_{\text{INR,n}}[k]$
  Calculate $\text{CINR}_{\text{min,n}}$ from (10)
  Calculate $\text{INR}_{\text{max,n}}$ using CNR_n from (11)
  if $\text{INR}_{\text{sum,n}} \geq \text{INR}_{\text{max,n}}$ **then**
    Concatenate $v_{\text{INR,n}}$ as cell to $\mathcal{V}_{\text{INR}}$
    else
      Concatenate empty cell to $\mathcal{V}_{\text{INR}}$
Return V_{CNR}, $\mathcal{V}_{\text{INR}}$

signal, and noise components is given by

$$\begin{aligned} y(t) &= y_x(t) + y_i(t) \\ &= x(t)\sqrt{\text{CNR}} \\ &\quad + \sum_{k=1}^{\mathcal{K}_t} \left(i_k(t) e^{j2\pi(f_{c,k} - f_{c,\text{gso}})t} \sqrt{\text{INR}_k} \right) \\ &\quad + \zeta(t). \end{aligned} \tag{15}$$

Algorithm 2 Generating the Datasets

Input: V_{CNR}, $\mathcal{V}_{\text{INR}}$, $f_{\text{c,gso}}$, $f_{\text{c,k}}$, B_x, $B_{i,k}$, Data Generation Parameters, and GSO ModCods
Output: $Y_{\mathcal{A}}$, $Y_{\mathcal{F}}$
Initalize: $Y_{\mathcal{A}}$, $Y_{\mathcal{F}}$ as empty matrices
for $n \leftarrow 1$**to**N **do**
  Generate ζ_n, AWGN noise of length M_t
  Get CNR_n, the value of $V_{\text{CNR}}[n]$
  Generate $x_n(t)$ from (12) at ModCod matching CNR_n
  Generate $y_{x,n}(t)$ from (14a)
  Get the $v_{\text{INR},n}$ vector, the cell of $\mathcal{V}_{\text{INR}}[n]$
  if $v_{\text{INR},n}$ *is an empty cell* **then**
    Set: $\alpha_n = 0$, interference-free label
    Set: $y_{i,n}(t)$ as zeros array
    else
      Set: $\alpha_n = 1$, interference label
      Initialize: $y_{i,n}(t)$ as zeros array
      for $k \leftarrow 1$**to**$\mathcal{K}_n$ **do**
        Get INR_k, the value of $\text{v}_{\text{INR},n}[k]$
        Generate $i_k(t)$ from (13) at a defined LEO ModCod
        From (14b), $y_{i,n}(t) \leftarrow y_{i,n}(t) + \left(i_k(t) e^{j2\pi(f_{c,k} - f_{c,\text{gso}})t} \sqrt{\text{INR}_k}\right)$
  Get $y_n(t)$ from (14)
  Get $y_n^{\mathcal{A}}$ of length M_t from (16)
  Concatenate $[y_n^{\mathcal{A}}, \alpha_n]$ to $Y_{\mathcal{A}}$
  Get $y_n^{\mathcal{F}}$ of length M_f from (17)
  Concatenate $[y_n^{\mathcal{F}}, \alpha_n]$ to $Y_{\mathcal{F}}$
Return $Y_{\mathcal{A}}$, $Y_{\mathcal{F}}$

At the analog-to-digital (A/D) conversion process, the received baseband signal is sampled at a frequency $f_s = \frac{1}{T_s}$ Hz, where T_s denotes the sampling duration. The number of samples per symbol of the desired $x(t)$ signal is $s_1 = \text{ceil}(\frac{T_x}{T_s})$, and the number of samples per symbol of the interfering $i_k(t)$ signal is $s_2 = \text{ceil}(\frac{T_{i,k}}{T_s})$. To avoid a potentially high sampling rate and the corresponding large number of samples for each symbol, we assume that the signal is sampled in its baseband form. In particular, in our analysis, the bandwidths $B_{i,k}$ and B_x are similar, implying that both GSO and LEO employ an identical bandwidth value. When the received signal is shifted by $f_{c,\text{gso}}$ in the baseband, its highest frequency component is B_x. The minimum sampling frequency required to capture the entire subband spectrum is $f_{s,\text{min}} = 2B_x$.

Although (14) is a time-domain signal, our work will consider both time and frequency-domain input signals. Both the IQ time-domain and frequency-domain representation are of complex type, which is not accepted as input to ML models. Regarding the time-domain IQ samples of $y(t)$, we transform them into 1-dimensional (1D) data, or a sequence, which can be used for training and testing. In a time instant n a

time-domain representation ($y_n^{\mathcal{A}}$) of the signal $y_n(t)$ can be generated by taking the magnitude[3] of the signal as follows

$$y_n^{\mathcal{A}} = |y_n(t)|, \tag{16}$$

where $y_n^{\mathcal{A}} \in \mathbb{R}^{M_t}$ is a vector with M_t elements of amplitude (A) values and it represents the time-domain representation of the signal $y_n(t)$. For simplicity, we refer to the time-domain representation as *Signal*. The frequency-domain representation ($y_n^{\mathcal{F}}$) is based on the fast Fourier transform (FFT), and can be obtained by generating the estimated power spectral density (PSD) of $y_n(t)$ using the Welch method [29]. This step can be formulated as follows

$$y_n^{\mathcal{F}} = 10log_{10}(\varphi(y_n(t))), \tag{17}$$

where φ is the equivalent `pewlch` function in MATLAB, and $y_n^{\mathcal{F}} \in \mathbb{R}^{M_f}$ is the PSD estimation vector for the IQ samples of $y_n(t)$, with M_f elements of decibels per Hertz (dB/Hz) values. For simplicity, we refer to the frequency-domain representation as *Spectrum*.

III. DATA PREPARATION

Before diving into the description of the proposed models for NGSO interference detection, in this section we present how the link budget and the received signal model presented in Section II, are used to generate a realistic dataset for training and evaluation.

Due to the need to calculate realistic CNR and INR values for generating the training and evaluation data, we first run a satellite simulation scenario with one GSO and multiple LEOs using MATLAB satellite toolbox [30]. The real-time positions and trajectories information of the GSO and LEO satellites are based on Kepler's six orbital elements. These can be easily extracted from the corresponding satellite two-line element (TLE) information that is publicly available on the celestrak website [31]. The corresponding orbit propagation of the selected LEO satellite has been calculated using MATLAB built-in functions, which provide estimates of latitude, longitude, and altitude over time according to the satellite trajectory. Using this setup in simulating satellites' interference scenarios where we consider the physical environment (distances, angles, satellites' orbit propagation, etc.), propagation conditions (path loss, weather, etc.), and the operational conditions (frequency, bandwidth), each element can drastically affect signal integrity and interference levels, altering CNR and INR values. Thus, considering all these factors allows us to generate more realistic link budget values and datasets, to fill the lack of real datasets in this specific domain [32], and which we believe are better than generating data from fixed CNR and INR values.

The simulation runs for a period of $\mathcal{T}$, and at each simulation step $\Delta(\tau)$, a sample of CNR, INR_k values are calculated from (1) to (9), and only values that exceed the INR threshold $\text{INR}_{\max}$ in (11) are saved. In general, we capture a total of N samples of CNR and INR values, within the time period $\mathcal{T}$. The overall data generation process is thus composed of two steps:

- CNR and INR values per-time instant calculation (see Algorithm 1).
- Detailed data generation of received signals (see Algorithm 2).

Algorithm 1. summarizes the calculations CNR and INR for each time instant. It outputs two vectors, the first $V_{\text{CNR}} \in \mathbb{R}^N$ is a vector consisting of all GSO CNR values calculated for each simulation step (time instant) indexed by n. The second output is a cell array $\mathcal{V}_{\text{INR}}$, each nonempty cell can be denoted as $\mathcal{V}_{\text{INR}}[n] \in \mathbb{R}^{\mathcal{K}_n}$, and it contains a vector $v_{\text{INR,n}}$ with $\mathcal{K}_n$ elements, each element representing a INR_k value of the k^{th} LEO that affects GSO communication with GGS at the n^{th} time instant.

The Algorithm 2 expresses the data generation steps of the received signals. It outputs two separate datasets generated for N samples, which are: 1) The dataset of the received signals in time-domain representation (Signal dataset) $Y_{\mathcal{A}} \in \mathbb{R}^{N \times M_t + 1}$, and 2) The dataset of the received signals in frequency-domain representation (Spectrum dataset) $Y_{\mathcal{F}} \in \mathbb{R}^{N \times M_f + 1}$. The additional variable $\alpha_N \in \mathbb{Z}_2$ is a binary indicator for when GGS receives an interference signal, in particular when GGS receives an interference-free signal α_n takes a value of 0. In contrast, when interference is present within the signal, α_n takes 1. Please note that α_n is not needed for the interference detection per-se but it is required for the evaluation of the different models (i.e., ground truth).

IV. INTERFERENCE DETECTION MODELS

The proposed models process 1D data based on the concepts of unsupervised learning. In this section, the models details are presented and discussed.

A. NOTATION AND ASSUMPTIONS

For readability purposes, we denote a single 1D input data (vector of length M) to the models as

$$y_n = \begin{cases} y_n^{\mathcal{A}}, & \text{for a time-domain (Signal) data} \\ y_n^{\mathcal{F}}, & \text{for a frequency-domain (Spectrum) data} \end{cases}$$

where $y_n \in \mathbb{R}^M$, $n \in [1, N]$, and $M \in \{M_t, M_f\}$. Furthermore, an element-wise normalization is performed on the input before it is fed to the models; this can be expressed as follow

$$y_{n,\text{norm}} = \frac{y_n - \text{a}}{\text{b} - \text{a}}, \tag{18}$$

where $y_{n,\text{norm}}$ is the normalized version of y_n of scale ranging from 0 to 1, a and b are the minimum and maximum values in the processed data representation, respectively. The subscript "norm" will be removed for readability, but the input y_n from now onwards is assumed to be normalized.

The goal of the proposed interference detection models is to learn an efficient and meaningful representation of the

[3]Preliminary testing showed that the magnitude component was bringing good results and such results did not improved when adding the phase component. Therefore, in this study, only the magnitude is considered.

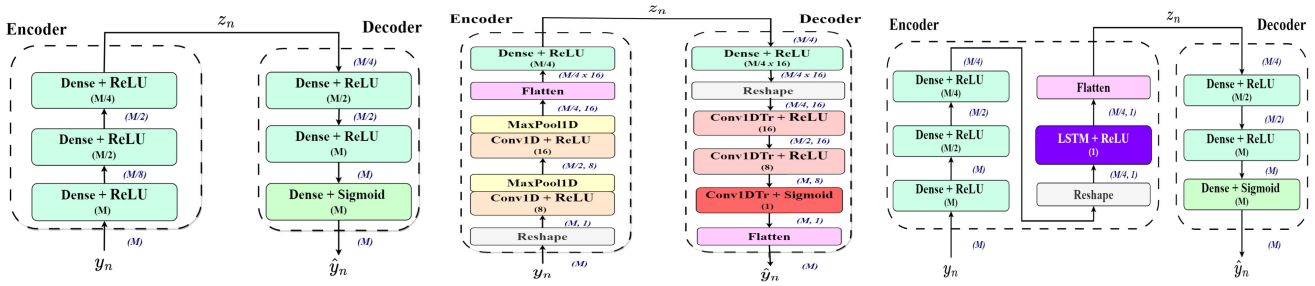

(a) AE Interference Detection Model (b) CAE Interference Detection Model (c) LSTMAE Interference Detection Model

FIGURE 3. Benchmark models.

input data by minimizing the reconstruction error between the original input (y_n) and a reconstructed output ($\hat{y}_n \in \mathbb{R}^M$). The interference detection problem is performed as an anomaly detection task [33]. An interference-free (anomaly-free) data consist of a GSO signal and noise only. A signal containing an anomaly (interference) from LEO consists of a GSO signal, noise, and LEO signals as interference. The mean absolute error (MAE) is the loss function that is used to evaluate the performance of all proposed models. In a noisy and interference data, the MAE loss function is robust to outliers and treats all errors with equal importance, this uniform treatment helps ensure that no single large error (outlier) can dominate the loss calculation, which is particularly beneficial in the context of interference detection where the goal is to identify all instances that deviate from the normal pattern of the data. MAE loss is calculated as the average of the absolute differences between the predicted values and the actual values and is given by the formula

$$\mathcal{L}_{\text{MAE}} = \frac{1}{N}\sum_{n=1}^{N} |\hat{y}_n - y_n|. \tag{19}$$

The expectation is that the proposed models will reconstruct interference-free sequences with a low MAE, and when interference data is received, this will be compared with the expected one and that would raise higher MAE. By setting a threshold β on the MAE loss, it is possible to differentiate between normal and interference observations, thus β serves as the interference score, and so on.

$$d_n = \begin{cases} 1 & \text{Interference}, \quad \text{if} \quad \mathcal{L}_{\text{MAE}} > \beta \\ 0 & \text{Interference-free}, \quad \text{otherwise} \end{cases} \tag{20}$$

where d_n is the model predication decision of the input y_n after being judged by the thresholding process.

B. BENCHMARK MODELS

Here we present and redesign three AE-based interference detection models, which are AE [25], CAE [12], and LSTMAE [24], as shown in Fig. 3, and will serve as a benchmark models to compare with our proposed models.

An AE-based model takes any input y_n and compresses it into a lower-dimensional representation vector $z_n \in \mathbb{R}^{M_z}$ ($M_z = \frac{M}{4}$) using an Encoder $\mathcal{E}(\cdot)$ as

$$z_n = \mathcal{E}(y_n). \tag{21}$$

A reconstructed version of y_n can be found by decoding the representation vector back to the original dimension by the Decoder $\mathcal{D}(\cdot)$ as

$$\hat{y}_n = \mathcal{D}(z_n). \tag{22}$$

Fig.3a shows a standard AE architecture, with a modified architecture compared to the one proposed in [27]. Excluding the input layer, the model comprises a total of five fully connected dense layers with a rectified linear unit (ReLU), and a final dense layer with a Sigmoid functions to ensure the output values fall between 0 and 1, this is useful for the normalized input data. The dense layers are adept at capturing linear relationships and basic patterns within the interference-free signal signal. By learning to compress and accurately reconstruct the typical GSO signal, the AE model can be used to establish a baseline of interference-free signal behavior.

Fig.3b illustrates a modified architecture of the CAE model proposed by [12]. CAE adapts convolutional ability to the AE architecture, which leverages feature extraction from input data with spatial or temporal structures. The encoder's convolutional (Conv1D) and max pooling (MaxPool1D) layers first perform dimensional reduction to encode the input sequence into the representation vector dimensions. The decoder layers then use conventional transpose layers (Conv1DTr) to up-sample the sequence dimensions, and the last Conv1DTr layer with M filters and a single kernel produces a single feature map, which then flattened to produce the reconstructed output. All layers use ReLU activation, except the last one with Sigmoid activation. The CAE can capture local patterns with shared weights (kernels), making it more efficient than dense layers for high-dimensional GSO signals that may have inherent spatial correlations due to modulation techniques. NGSO interference would likely disrupt these spatial correlations, which the CAE would manifest as increased reconstruction errors.

Fig.3c illustrates the architecture of the LSTMAE model, it combines dense layers with an LSTM unit on the encoder to process the representation vector of the input sequence, which is suitable for learning order dependence in sequence data prediction problems, and it is an improved architecture from that of [24]. The LSTM unit, a type of recurrent neural networks (RNNs), is particularly useful for sequence data

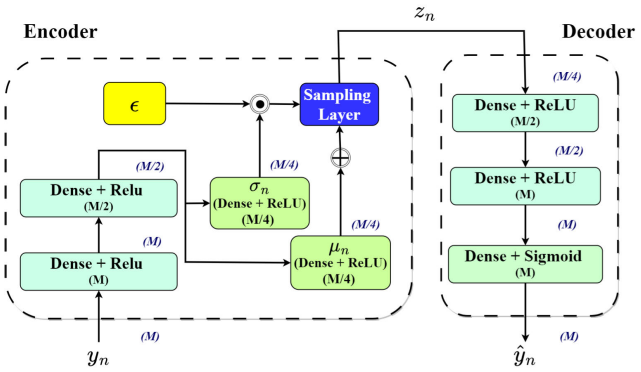

FIGURE 4. Variational autoencoder interference detection model (VAE).

where the current sequence is dependent on the previous sequence. This is particularly appealing for NGSO-to-GSO interference detection, where the expected GSO signal has a strong correlation with the previous GSO signal instance.

C. PROPOSED GenAI-Based MODELS

1) VARIATIONAL AUTOENCODER MODEL (VAE)

Our first proposed GenAI-based model is the VAE model, its architecture illustrated in Fig. 4. VAE learns not only the encoding of the data, but also the underlying probability distribution [14].

As an architecture, VAE consists of similar hyperparameters in the encoder and decoder parts as in the standard AE. The major difference lies in the encoder and the representation vector part. Here, VAE learns to generate new sequences that are similar to the input sequence by enforcing a distribution on the representation vector. This is achieved by introducing a sampling layer instead of a typical neural layer. This layer samples from the distribution defined by the mean (μ_n) and standard deviation (σ_n) dense layers. Furthermore, the reparameterization trick is utilized in VAE, which entails expressing the representation vector as a deterministic function of learnable parameters and a fixed distribution sample. This technique effectively decouples the stochastic element from the parameters optimization process. The reparameterization trick is represented by the equation

$$z_n = \mu_n + \sigma_n \odot \varepsilon, \tag{23}$$

where μ_n and σ_n are learnable parameters, and ε is a sample of a standard Gaussian distribution. The symbol $\odot$ represents the Hadamard product, or element-wise multiplication, which facilitates the combination of the variability introduced by ε with the scaled parameter σ_n. The form in (23) of z_n allows differentiation with respect to the parameters μ_n and σ_n while incorporating randomness, thereby allowing the loss gradient to be backpropagated through the stochastic sampling process.

Let $p(y)$ denote the actual training data distribution, $p(z)$ express the distribution of the representation vector, and $p(\hat{y}|z)$ indicate the conditional distribution of data reconstruction -generation- given the representation vector. The goal of VAE is to infer $p(z)$ from $p(z|y)$. The distribution $p(z|y)$ is a complex probability distribution that positions the input data in a representation vector, which is typically a standard Gaussian distribution $\mathcal{N}(0, 1)$. However, lacking the actual distribution $p(z|y)$, we approximate it through a more tractable distribution $q(z|y)$, in this case as an approximation of the Gaussian distribution $\mathcal{N}(\mu, \sigma^2)$. During the VAE training process, the encoder is tasked with assimilating the approximate distribution $\mathcal{N}(\mu, \sigma^2)$ so that it closely resembles the true distribution $\mathcal{N}(0, 1)$. This resemblance is quantified using the Kullback-Leibler (KL) divergence [34], as a metric of disparity between two probability distributions. The loss function for the VAE inherently incorporates this KL divergence term, which it strives to minimize as

$$\mathrm{D_{KL}}\left[q(z|y)||p(z|y)\right] = \int q(z|y) \log \frac{q(z|y)}{p(z|y)}\, dz. \tag{24}$$

In this case, $\mathrm{D_{KL}}$ can be derived as [14]

$$\mathrm{D_{KL}} = -\frac{1}{2}\left(1 - \mu^2 - \sigma^2 + \log(\sigma^2)\right). \tag{25}$$

VAE probabilistic approach allows it to generate new sequences that are variations of the input data, potentially offering a more robust detection of NGSO interference by evaluating how likely a new signal instance could have been generated by the same distribution as the GSO signal. Diffrent from the benchmark models, the loss function of the VAE incorporate the KL divergence $\mathrm{D_{KL}}$ term, or the similarlty loss as follows

$$\mathcal{L}_{\mathrm{VAE}} = \frac{1}{N}\sum_{n=1}^{N} |\hat{y}_n - y_n| + \mathrm{D_{KL}}, \tag{26}$$

The loss function of the VAE is composed of two main components: the reconstruction error, using $\mathcal{L}_{\mathrm{MAE}}$, and a regularization term $\mathrm{D_{KL}}$, which accounts for the divergence in the representation vector distribution approximations. The integration of $\mathrm{D_{KL}}$ within the VAE loss function can be interpreted as a measure of how well the representation vector matches the desired standard normal distribution, ensuring that the model generates meaningful and diverse data samples. Additionally, this regularization aids in curbing overfitting throughout the model training process.

2) TRANSFORMER-BASED INTERFERENCE DETECTOR MODEL (TRID)

Inspired by transformer models [15], we propose the TrID model as illustrated in Fig. 5. Unlike VAEs, which sample probability distributions to generate new data, transformer models are particularly adapted for GenAI applications because of two mechanisms: self-attention and positional encodings. Both of these technologies allow the model to focus on how sequences are related to each other over a long time [15].

Our proposed TrID model consists of three main blocks. At the beginning, the input signal is passed through Convolutional Front-end where two conv1D layers with ReLU

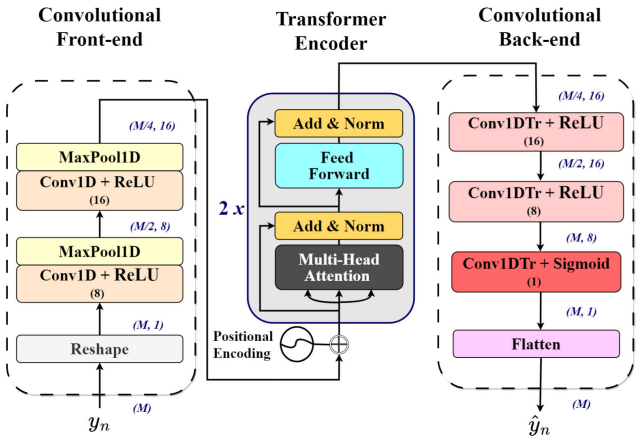

FIGURE 5. Transformer-based interference detector model (TrID).

activation and each is followed by MaxPool1D. The Convolutional Front-end primarily serves to extract meaningful features from the raw input signal, reducing dimensionality while reducing the computational load, and helping in bridging the local features with the global context needed for the transformer layers. This is very important for understanding the underlying structure of the data. This setup ensures that the transformers are not merely processing raw data but rather more abstract representations of the input signal.

The second block is Transformer Encoder, which consists of a sinusoidal positional encoding followed by two standard transformer encoder layers [15]. The abstract representation, which has the dimensions $\frac{M}{4} \times 16$, of the input signal is treated as a sequence of embeddings (sequence length $\times$ embedding size), a Positional Encoding is applied before the first transformer layer to encode the embedding order of the input sequence and get,

$$PE_{(pos,2i)} = sin(pos/1000^{2i/d_{TrID}}), \tag{27}$$

$$PE_{(pos,2i+1)} = cos(pos/1000^{2i/d_{TrID}}), \tag{28}$$

where pos is the embedding position in the sequence, i is the dimension in the embedding space and d_{TrID} is the dimensionality of the embedding or the embedding size. That is, each dimension of the positional encoding corresponds to a sinusoid. Next, the first transformer's multi-head attention is applied on the positional encoding output. Toward that, we consider the linear projections of the queries Q, the keys K, and the values V, then we obtain the attention matrix as

$$Att\,(Q, K, V) = softmax\left(\frac{QK^T}{\sqrt{d_k}}\right)V, \tag{29}$$

where d_k represents the dimension of the keys. If the number of attention heads is h, and the output weight matrix is denoted as W^l_{out}, the output of the multi-head attention is given as

$$MH\,(Q, K, V) = Concat\,(H_1, \ldots, H_h)\,W_{out}, \tag{30}$$

where

$$H_i = \left(QW_i^Q, KW_i^K, VW_i^V\right), \tag{31}$$

where W_i^Q, W_i^K, W_i^V are the weight matrices of each head's inner dense layers, and W_{out} is the final dense layer weight matrix. In this paper, $W_i^Q \in \mathbb{R}^{d_{TrID} \times d_k}$, $W_i^K \in \mathbb{R}^{d_{TrID} \times d_k}$, $W_i^V \in \mathbb{R}^{d_{TrID} \times d_v}$, where $d_v = d_k = \frac{d_{TrID}}{h}$.

In the self-attention mechanism of a transformer, the internal relationships within an input sequence are comprehensively learned. Essentially, attention weights are calculated at each sequence position by comparing a given position with every other position in the sequence. This process allows the model to capture the overall sequence information, enhancing the representation of each observation by focusing on the contributions of all other positions. Consequently, the hidden state of each point in the sequence emphasizes the contextual significance of the surrounding regions to that specific point.

The output of the multi-head attention are added and normalized before process by a feed forward network (FFN) with residual connection, followed by addition and normalization once again in order to obtain the final output of the first transformer encoder layer. This layer processes the embedding sequence input to create a unified hidden representation for each position within the sequence. Subsequently, these representations are fed into a second transformer encoder layer, which iteratively helps generate more sophisticated, higher-level representations during training. This hierarchical processing enhances the model's ability to discern more complex patterns and relationships within the data.

The extracted features of the Transformer Encoder block are further processed with the third block, namely Convolutional Back-end. The Convolutional Back-end is consisting of transposed convolutional layers (two conv1D layers with ReLU, and a third conv1D layer with Sigmoid), and serves to up-sample these features back to the original dimensionality of the input in $\hat{y}_n$. The output of the convolutional layer is fed into the flattening layer where the final reconstructed signal $\hat{y}_n$ is conveyed. The Convolutional Back-end not only reconstructs the signal from the abstracted and generated representations from the Transformer Encoder block but also refines this reconstruction to ensure that the output is detailed and accurate. It effectively translates the global contextual understanding of the transformer back into a high-resolution space. TrID utilized the MAE loss function defined in (19).

D. INTERFERENCE DETECTION PERFORMANCE METRICS

Performance metrics provide quantitative measures that help to understand how well the model performs, particularly in distinguishing between different classes [35]. Here we introduce some of the selected metrics that will be used in this paper to evaluate the performance of the models, listed in Section IV.IV-B, for the interference detection task.

Let us first introduce the basic key performance indicators: 1) **True Positives** (TP): The number of interference (positive) instances correctly identified by the model, 2) **True Negatives** (TN): The number of interference-free (negative) data correctly identified by the model, **False Positives** (FP):

The number of interference-free data incorrectly identified as interference, and 4) **False Negatives** (FN): The number of interference data incorrectly identified as interference-free observations. The derived metrics includes

- True Positive Rate (TPR): Also known as Recall, or the probability of detection (P_D). This metric measures the proportion of actual interference instances that are correctly identified by the model.

$$\text{TPR} = \frac{\text{TP}}{\text{TP} + \text{FN}}. \tag{32}$$

- False Negative Rate (FNR): It indicates the proportion of actual interference instances that are missed identified by the model as interference-free instances. Is the complement of the TPR.

$$\text{FNR} = \frac{\text{FN}}{\text{TP} + \text{FN}}. \tag{33}$$

- True Negative Rate (TNR): This metric measures the proportion of actual interference-free instances that are correctly identified as such by the model.

$$\text{TNR} = \frac{\text{TN}}{\text{TN} + \text{FP}}. \tag{34}$$

- False Positive Rate (FPR): This metric measures the proportion of actual interference-free instances that are incorrectly identified by the model, in other words it indicates the probability of false alarms. Is the complement of the TNR.

$$\text{FPR} = \frac{\text{FP}}{\text{TN} + \text{FP}}. \tag{35}$$

- Normalized-valued Confusion Matrix (NCM): NCM is a tabular representation of TNR, FPR, and FNR and TPR, widely used in classification problems [35].
- Accuracy score: It represents the overall proportion of correct predictions (both TP and TN) relative to the total number of cases examined.

$$\text{Accuracy} = \frac{\text{TP} + \text{TN}}{\text{TP} + \text{TN} + \text{FP} + \text{FN}}. \tag{36}$$

- Precision score: This metric measures the proportion of predicted interference that are actually TP. It focuses on the purity of interference identifications. Precision is particularly important in contexts where the cost of false alarm is high.

$$\text{Precision} = \frac{\text{TP}}{\text{TP} + \text{FP}}. \tag{37}$$

- F1 Score: F1 score is the harmonic mean of precision and recall. This score is a robust metric for evaluating interference detection models because it accounts for both the model's ability to correctly identify interference and its efficiency in not misclassifying interference-free signals as interference.

$$\text{F1} = 2 \times \frac{\text{Precision} \times \text{Recall}}{\text{Precision} + \text{Recall}}. \tag{38}$$

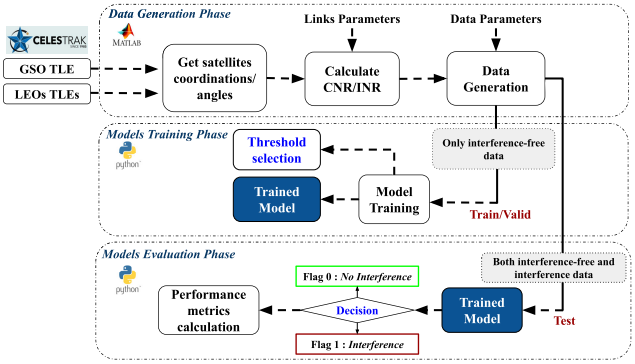

FIGURE 6. Schematic overview from data generation to models training and evaluation.

- Receiver Operating Characteristic Curve (ROC): ROC is a graphical representation that plots TPR against FPR at various threshold settings.
- Area Under the ROC Curve (AUC): AUC score is a scalar value summarizing the ROC curve. AUC is a valuable metric for evaluating the performance of interference detection models [36], it gives a sense of how well the model can be tuned to balance the detection of interference (TPR) against mistakenly flagging interference-free instances as interference or false alarms (FPR).

V. SIMULATION RESULTS

In this section, we present the simulation setup, including details on the data generation, model training phase, as well as validating and comparison of the different ML models proposed in Section IV. The workflow logic is shown in Fig. 6. In this approach, data labeling (interference and interference-free) is only used to calculate the key performance metrics described in Section IV-D.

A. DATA GENERATION PHASE

We initialize our simulation in MATLAB by selecting one GSO satellite from the SES fleet, the ASTRA 28.2E system [37].The GGS is assumed to be a VSAT dish located in Luxembourg City, Luxembourg, Coordinates: (49.6257N, 6.1598E, 300 m). The GSO system corresponds to an European broadcasting system operating at 10.7-12.7 GHz [38]. The potential NGSO interference is emulated by selecting 20 LEO satellites that eventually fly in the neighboring area of the GSO line of sight. These correspond to 10 LEO satellites from SpaceX Starlink constellation, and 10 LEO satellites from Eutelsat-OneWeb constellation. Note that the altitudes of these LEO satellites are between 550 and 1,200 Km. Starlink and OneWeb constellations are deployed to provide broadband connectivity worldwide, and according to recent filings with the Federal Communications Commission (FCC), Starlink OneWeb satellites are operating in the same Ku frequency bands 10.7-12.7 GHz as ASTRA [39], [40].

TABLE 1. Simulation setup and link budget parameters (Algorithm 1).

Parameters	Names	Values
-	Simulation UTC startTime	30-Jul-2023 00:00:00
-	Simulation UTC stopTime	01-Aug-2023 00:00:00
$\mathcal{T}$	Simulation period	48 Hours
$\Delta\tau$	sampleTime	10 Seconds
N	Simulation samples	17281
-	GSO satellite TLE	1 TLE
-	LEO satellites TLEs	20 TLEs
L_{AD}	Link additional losses	0 to 9 dB
GSO satellite Parameters		
$EIRP_{\text{gso}}$	Transmitted EIRP	52.2 dBW
B_x	Signal bandwidth	50 MHz
$f_{c,\text{gso}}$	Carrier frequency	11.750 GHz
e_r	maximum BER allowed [42]	10^{-5}
LEO satellites Parameters (Per Satellite)		
$EIRP_k$	Transmitted EIRP	44.7 dBW
$B_{i,k}$	Signal bandwidth	50 MHz
$f_{c,k}$	Carrier frequency of LEO	11.750 GHz
B_{overlap}, k	Overlapping bandwidth	50 MHz
B_{adj}, k	Adjustment factor	1
GGS Parameters		
D_A	Antenna diameter	1.2 m
e_A	Antenna efficiency	0.6
λ_{gso}	Wavelength	0.0255 m
T_{temp}	Noise temperature	250° K
$G_{r,\text{gso}}(\theta_0)$	GSO recivng gain, from (6)	42.2 dBi

1) SIMULATION SETUP AND LINK BUDGET CALCULATION

Table 1 describes the simulation setup and link budget parameters used in Algorithm 1 for the computation of CNR and INR values. Satellite communications implement the air interface defined in the DVB-S2X standard for downlink transmission. The DVB standard defines a set of ModCod schemes that adapt the transmission mode depending on the link characteristics. In our simulation, the value of the link losses (L_{AD}) is intentionally varied over time within the range of [0,9] dB to emulate different ModCod schemes for both GSO and LEO links independently.

A representation part of the visibility intervals of GSO and LEOs satellites to the GGS during the simulation is shown in Table 2. It can be observed that the selected GSO satellite (ASTRA 2F) is visible to GGS all the time with a total duration of 48 hours (172800 seconds, which corresponds to the overall simulation period), while the selected LEO satellites have discrete visibility to GGS occurring 296 times during the whole simulation period, with varying visibility duration (190 to 1190 seconds).

With this setup, Algorithm 1 generates a total of $N = \frac{48\times60\times60}{10} = 17281$ simulation samples. We recorded 2218 data points whose aggregated interference over noise ratio exceeds the INR threshold INR_{max} defined in (11). The maximum aggregated interference over noise ratio is $\text{INR}_{\text{sum}}[\text{dB}] = 32.47$ and the minimum is $\text{INR}_{\text{sum}}[\text{dB}] = 4.49$. Regarding individual interference over noise ratio (INR per LEO satellite), we obtain maximum $\text{INR}_k[\text{dB}]$ value of 32.47,[4] and the minimum $\text{INR}_k[\text{dB}]$ value is -31.03. For the GSO satellite link, the maximum CNR[dB] value is 15.40, and the minimum CNR[dB] is 6.40.

TABLE 2. The visibility of GSO and LEOs to the GGS.

Source	Target	IntervalNumber	StartTime	EndTime	Duration
ASTRA 2F	GGS	1	30-Jul-2023 00:00:00	01-Aug-2023 00:00:00	172800
STARLINK-2734	GGS	1	30-Jul-2023 09:02:20	30-Jul-2023 09:05:30	190
STARLINK-2734	GGS	2	30-Jul-2023 10:36:20	30-Jul-2023 10:47:40	680
...	...	...	...	...	...
ONEWEB-0101	GGS	19	31-Jul-2023 18:03:00	31-Jul-2023 18:09:50	410
ONEWEB-0101	GGS	20	31-Jul-2023 23:45:40	01-Aug-2023 00:00:00	860

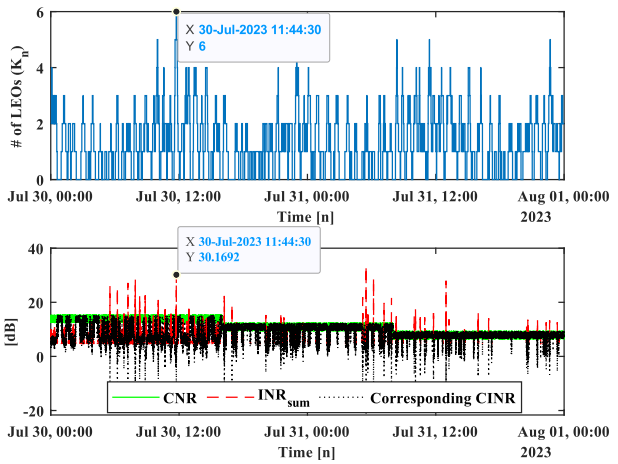

FIGURE 7. Plot of numbers of LEO satellites interfering GGS (Top), and the received CNR and INR_{sum} (Bottom), over the simulation period.

Fig. 7 illustrates how the simulation and the calculation of CNR, INR are performed in parallel. The top plot visualizes the varying number of LEO satellites received as interference at GGS for each time instant n. The bottom plot illustrates CNR[dB] and $\text{INR}_{\text{sum}}[\text{dB}]$ that exceed the INR threshold INR_{max} mentioned above in (11).

Fig. 8 shows the GGS radiation pattern described in (5) and the gain of each satellite access to it at the 4227^{th} time instant (i.e., at 30-07-2023 11:44:30). It can be seen that satellite LEO_1 is received with a significantly higher gain than the rest of the LEO satellites.

2) RECEIVED SIGNALS DATA GENERATION

To generate data from the received signals for training and evaluation as described in Algorithm 2, we implement the parameters shown in Table 3, and the table of simplified modulation schemes from [19] as in Table 4.

[4]During the simulation, the maximum aggregated interference at the GSO ground station was primarily caused by significant in-line interference from a LEO satellite, while another LEO contributed with a close-to-negligible interference power.

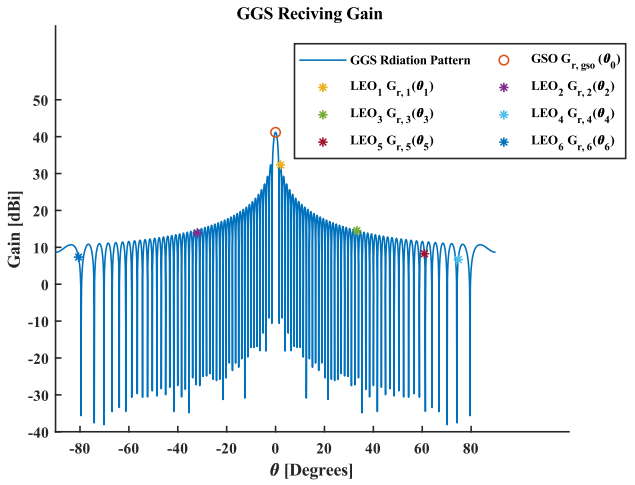

FIGURE 8. Visualization of the GGS receiving gain of each satellite accessing to GGS at 30-07-2023 11:44:30.

TABLE 3. Data generation parameters (Algorithm 2).

Parameters	Names	Values
f_s	Sample frequency	100 MHz
s_1, s_2	Number of samples per symbol	2 samples
V_x, V_i	Number of symbols per signal	400 symbols
M_t	Total Number of samples per signal	800 samples
-	LEO ModCod	QPSK
-	p_{RC_x} and p_{RC_i} Roll-off factor	0.25

TABLE 4. GSO ModCods.

ModCod	CNR required [dB]
QPSK	≤ 6.6
8PSK	> 6.6 & ≤ 9.0
16APSK	> 9.0

With this parameter set-up, Algorithm 2 generates two sets of data, the time-domain Signal dataset, and the frequency-domain Spectrum dataset as described in Section III. The Signal dataset ($Y_{\mathcal{A}}$) has dimensions of $N \times M_t = 17281 \times 800$ after excluding the label column $\alpha \in \mathbb{Z}_2^N$. Due to the fact that the FFT signal bandwidth covers the spectrum $[-\frac{f_s}{2}, \frac{f_s}{2}]$ in baseband, and the number of frequency bins in the frequency domain is equal to the number of samples in the time domain, thus the Spectrum dataset $Y_{\mathcal{F}}$, has the dimensions of $N \times M_f = 17281 \times 800$ after excluding the label column $\alpha \in \mathbb{Z}_2^N$. In this case, both datasets have the same dimensions $N \times M$, where $M \in \{M_t, M_f\}$.

As mentioned in Section IV-A, the input layer in each model takes a vector (sequence) y_n with length M, where n indicates the sample index within N data points (sequences).

The label α_n indicating the presence and absence of interference is only used to ensure that the models are trained only with the expected GSO signal. Consequently, the final data distribution used for training and testing is as follows: 1) The Training Set, composed exclusively of $10,397 \times M$ interference-free dats; 2) The Validation Set, containing $1,175 \times M$ interference-free data; and 3) The Testing Set, contains $2,907 \times M$ interference-free data and all $2,802 \times M$ interference data.

B. MODELS TRAINING PHASE

Tensorflow and Keras frameworks are used to build the models proposed in Section IV-B in Python. All models are compiled with MAE as the main loss function, and Nesterov implemented Adam as the optimizer. The weight and base parameters were updated using the interference-free Training Set, and the results were validated using the Validation Set. The experiments in the following parts were carried outusing the HPC facilities of the University of Luxembourg [42]. Thanks to these facilities, 60-core CPU units with 3 TB RAM memory are used.

1) MODELS TRAINING

Each model inputs y_n, after a normalization step using the maximum and minimum values found on the Training Set as explained in (18). Each AE-based models, including VAE, reduced the dimensionality of the input from $M = 800$ in y_n, to $M_z = 200$ in z_n, each layer parameters and structures can be seen in Fig. 3 and Fig. 4. For the TrID model, Fig. 5, in the Transformer Encoder we apply $h = 4$ parallel attention layers, $l = 2$ transformer encoder layers, and all the sub-layers, including the positional encodings, produce output of dimensions $\in \mathbb{R}^{\frac{M}{4} \times d_{TrID}}$, with $d_{TrID} = 16$.

The models were trained for 30 epochs with a batch size of 64. The model training phase is shown in Fig. 9. First, Fig. 9a shows the MAE loss over 30 epochs of training for the Signal dataset. The x-axis represents the epoch number, and the y-axis represents the MAE loss. A lower MAE indicates better reconstruction performance, as the error between the model predictions and the actual data is smaller. AE, LST-MAE, and VAE models seem to converge quickly, with most of the loss reduction occurring in the first few epochs, CAE converges after, and TrID converges at a significantly lower MAE value than the other models. This suggests that the TrID model learns the patterns in the time-domain data more efficiently. Except for TrID, all other models show a sharp decline in loss initially, which flattens as the epochs increase, indicating that they have quickly reached a point of minimal improvement in error reduction. Similarly, Fig. 9b shows the MAE loss over 30 epochs of training for the Spectrum dataset. The models training behavior is quite similar to that of the Signal dataset, with all models showing rapid convergence in the initial epochs, except TrID and CAE. Compared to the Signal dataset training, the loss values for the Spectrum dataset are lower overall, which may suggest that the models struggle a bit to capture the patterns in the data in the time-domain or that it is inherently more complex.

In Fig. 9c, the bar chart compares the number of trainable parameters across the models, which is the same for both Signal and Spectrum datasets. Generally, a model with more

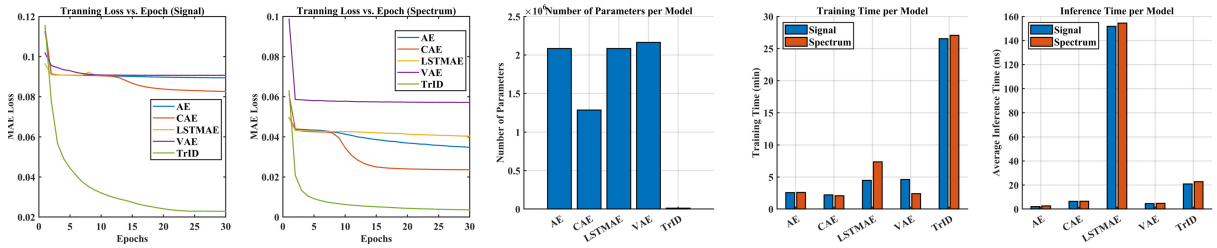

(a) Loss-Epochs (Signal) (b) Loss-Epochs (Spectrum) (c) No. Parameters per model (d) Training Time per model (e) Inference Time per model

FIGURE 9. Training phase results.

parameters can capture more complex patterns, but may also be prone to overfitting and may require more data to train effectively. AE, LSTMAE, and VAE models appear to have a similar number of parameters with their fully connected dense layers, while the models with convolutional layers seem to have a smaller number of parameters, with TrID being significantly the lowest. In satellite communication systems, where computing resources are often constrained, models with a large number of parameters can be impractical. They may require more memory and processing power, which could impact the efficiency of satellite systems.

Fig. 9d shows the training time for each model in minutes (min) for training both Signal and Spectrum datasets. Training time is important for practical consideration, since models that take longer to train can be more costly in terms of computational resources and time. Here, on both datasets, the TrID model trains the slowest compared to the other models, potentially due to the self-attention mechanism within the transformers, which despite its computational complexity, is an important layer for improving the model accuracy. Other models, while having more trainable parameters than the TrID, were quicker to train.

Fig. 9e shows the inference time for each model in milliseconds (ms) for both Signal and Spectrum datasets. It can be seen that LSTMAE takes the longest time (up to 160 ms) to reconstruct an input data, which could be due to the LSTM unit complexity. Despite having a longer training time, TrID took less time (up to 20 ms) to reconstruct the input data. AE and CAE, VAE were the most efficient in terms of inference time. Satellite communications often require real-time or near-real-time response to maintain system integrity and performance. Interference detection models with faster inference times can quickly identify and respond to potential issues, preventing further complications or system failures.

Fig. 10 shows the reconstruction performance of the models, each figure depicts input data (cyan color) alongside the reconstructed output (navy color) obtained and the reconstruction error area between them (golden color), after being rescaled back to the original values of amplitude or dB/Hz. It is observed that the reconstruction error is more pronounced in the data with interference, as indicated by the larger golden area, which is expected since the models were trained in interference-free data and interference would naturally be harder to reconstruct and thus easier to detect. Despite the

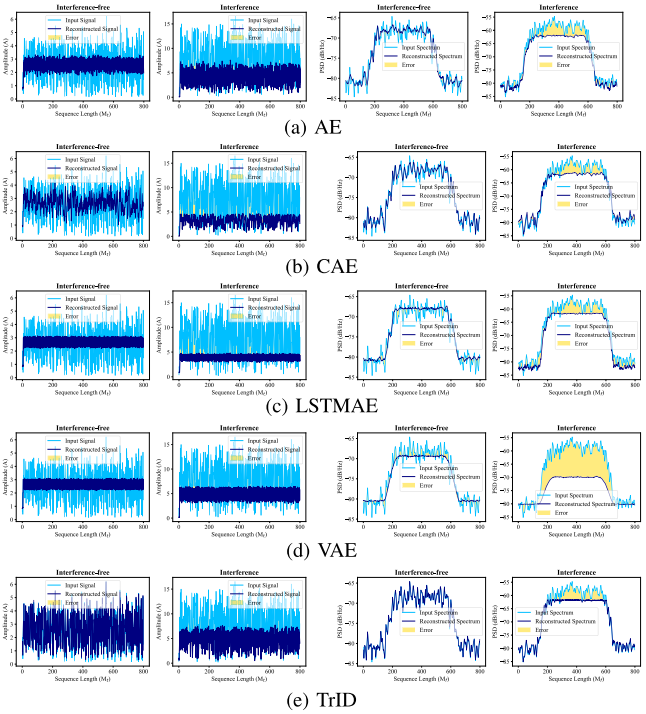

(a) AE
(b) CAE
(c) LSTMAE
(d) VAE
(e) TrID

FIGURE 10. Model input (cyan color), reconstructed output (navy color), and error area (golden color) for an interference-free and interference Signal data (sub-left figures) and Spectrum data (sub-right figures).

complexity of the training data,[5] the TrID model generates an interference-free data with minimal MAE error, indicating the possibility of utilizing the model for future data generation for the purpose of training deep learning models.

2) THRESHOLD SELECTION

As discussed in Section IV-A, by setting a threshold β on the training loss of each model and each dataset, it is possible to differentiate between interference-free and interference data. We propose to use an initial threshold value β_0 for each model and dataset, from the sum of the mean and two standard deviation of the MAE loss values on the training dataset $\mathcal{L}_{\text{MAE,Train}}$, and it can be derived using this equation

$$\beta_0 = \mu(\mathcal{L}_{\text{MAE,Train}}) + 2 \times \sigma(\mathcal{L}_{\text{MAE,Train}}) \tag{39}$$

[5]For training data of a single NGSO satellite, single SNR, and single ModCod [25], all models demonstrated perfect reconstruction performance.

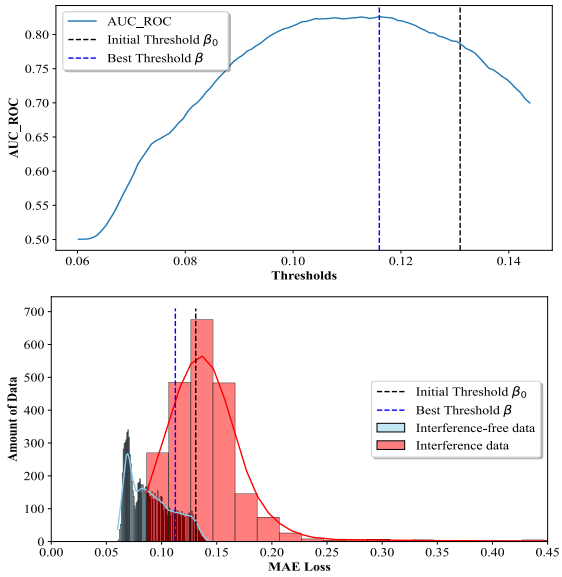

FIGURE 11. Threshold selection based on optimal AUC score approach.

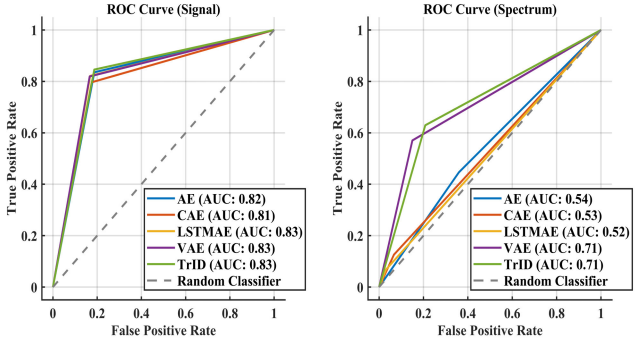

FIGURE 12. AUC_ROC plot per model for Signal data (left), and Spectrum data (right).

The initial threshold value has been derived with the objective of achieving satisfactory performance in the task of interference detection. However, as part of this paper's contribution, we extended the threshold definition to an enhanced threshold value (β) by examination of interference segments (assuming that these are available and have been previously identified as such). In particular, we first evaluate the classification performance of each model on a Testing Set that includes interference and interference-free data, iterating over a series of threshold values that are derived from the MAE losses values of the training dataset $\mathcal{L}_{\text{MAE,Train}}$. Subsequently, we pinpoint the optimal threshold value that yields the maximum AUC score. The choice of the AUC score is due to its ability to be tuned to balance the detection of interference, or the recall, while avoiding false alarms.

Fig. 11 illustrate an example of the initial threshold β_0 and the enhanced threshold β within the MAE Loss values (thresholds series) specifically derived for the VAE model and the Signal dataset.

TABLE 5. Models performance summary on signal test data.

Model	β	Accuracy	TPR	FPR	F1 Score	AUC
AE	0.1102	0.8239	0.8354	0.1874	0.8248	0.8240
CAE	0.1031	0.8107	0.7967	0.1754	0.8068	0.8106
LSTMAE	0.1125	0.8264	0.8215	0.1687	0.8244	0.8264
VAE	0.1127	0.8266	0.8192	**0.1661**	0.8242	0.8266
TrID	0.0223	**0.8318**	**0.8399**	0.1763	**0.8321**	**0.8318**

TABLE 6. Models performance summary on spectrum test data.

Model	β	Accuracy	TPR	FPR	F1 Score	AUC
AE	0.0355	0.5441	0.4463	0.3597	0.4928	0.5433
CAE	0.0268	0.5327	0.1262	0.0671	0.2114	0.5296
LSTMAE	0.0456	0.5219	0.0681	**0.0311**	0.1238	0.5185
VAE	0.0725	**0.7112**	0.5703	0.1501	0.6621	0.7101
TrID	0.0037	**0.7112**	**0.6294**	0.2083	**0.6838**	**0.7106**

C. MODELS EVALUATION PHASE

After training and selecting the threshold for each model and each data representation, we can now evaluate the trained models with the data from the Testing Set. We analyze the performance of these models in detecting NGSO interference at GGS based on the key performance indicators described in Section IV-D. Evaluation encompasses two different representations of received signals: time domain (Signal data) and frequency domain (Spectrum data). We present some classification performance plots for each model: Fig. 12 presents the ROC curves per model for the Signal dataset (right), and the Spectrum dataset (left), as well as highlighting the AUC scores within the figure labels. These ROC curves show the trade-off between the true positive rate and false positive rate for each model. The closer the curve follows the left-hand border and then the top border of the ROC space, the more accurate the model. Hence, the closer AUC is to 1, the better the model is at predicting true interference-free instances while minimizing false alarms. The models' performances vary significantly between signal and spectrum data. For signal data, LSTMAE, VAE, and TrID perform equally well and slightly better than AE and CAE. For spectrum data, the TrID and VAE clearly outperform the other models, indicating that their architectures may capture the complexities of the spectrum data better. The CAE and LSTMAE models do not adapt as well to the spectrum data, possibly due to limitations in how they capture and utilize features in this type of data.

Fig. 13 shows the normalized confusion matrices CM for all models and data representations. In addition, Table 5 and Table 6 summarize the results from Fig. 12 and Fig. 13, for the Signal dataset and the Spectrum dataset, respectively.

Starting with Table 5, TrID tends to lead in all metrics compared to other models, it has the highest Accuracy and AUC at 83. 18%, it also has a low false alarm rate or FPR at 17.63%, which is about 1% higher than VAE with the best value of 16.61%. On the other hand, LSTMAE and VAE show a closely identical performance with VAE being slightly better in Accuracy, FPR and AUC. AE and CAE while not

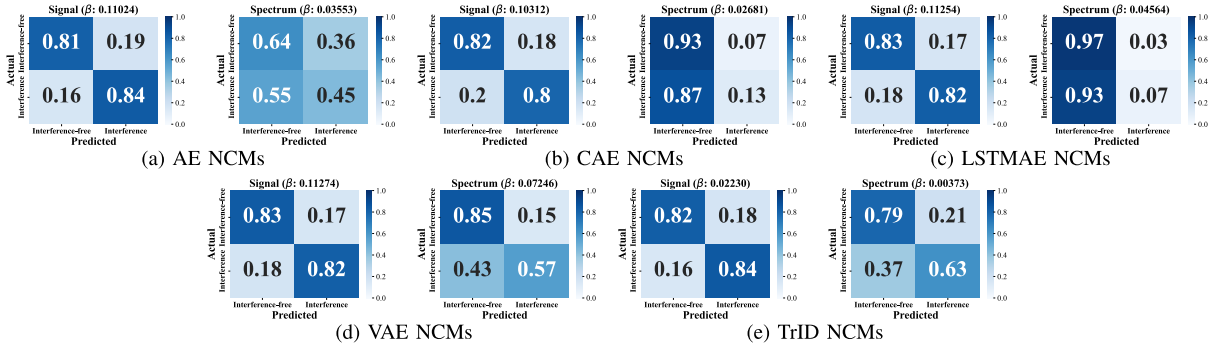

(a) AE NCMs (b) CAE NCMs (c) LSTMAE NCMs

(d) VAE NCMs (e) TrID NCMs

FIGURE 13. Normalized Confusion Matrices per model for Signal data (sub-left figures), and Spectrum data (sub-right figures).

leading in any specific category, they still perform reasonably well.

Regarding Table 6 for the Spectrum dataset, TrID and VAE models outperforms others, achieving the highest scores across all metrics, with +71% in AUC score, except FPR which LSTMAE and CAE were superior, however, this comes with a trade-off as their TPR are very low. VAE, although still performing well, falls slightly behind TrID in all metrics. All models show a marked decrease in performance metrics in the frequency-domain as compared to the time-domain, highlighting the complexity of detecting interference in the spectrum data.

As a conclusion for this evaluation, our proposed GenAI-based models (TrID and VAE) performed the best in both signal and spectrum data compared to the other models, with the highest Accuracy, F1Score, and AUC values. In applications where processing of both spectrum and signal data is required, VAE or TrID would be the preferable choice given their superior AUC scores. In real-world applications, the choice between TrID and VAE, or another model, might also be influenced by computational constraints, training time, inference times, and reconstructing ability, which depends on the application requirements and the resources available. Given the critical nature of detecting NGSO interference in GGSs, where missed detections and false alarms may have significant implications, a model with a strong balance between TPR and FPR is essential. Overall, TrID was superior and also the best model in terms of reconstructing the input data. Thus, the TrID model on time-domain Signal data representation is recommended for further investigations. Here are some insights on possible reasons why the TrID architecture shows better results than the AE, CAE, LSTMAE, and VAE:

- **Multi-Head Self-Attention Mechanism:** As mentioned in the model description, the self-attention mechanism in TrID allows for a dynamic weighting of the significance of different parts of the signal. Moreover, the global receptive field of self-attention enables the model to capture long-term dependencies without being restricted by the vanishing gradient problem in typical LSTM.
- **Enhanced Accuracy:** The inclusion of convolutional layers for post-processing and skip connections within the TrID architecture helps maintain gradient flow and adjust dimensionality. This contributes to a more accurate signal reconstruction and guards against issues such as vanishing gradients that can hinder training in deep networks.
- **Better Data Generation Capabilities:** When generating data, TrID often outperform VAE as they can model complex distributions without being constrained by the need to match a specific prior distribution, leading to a higher fidelity in the generated data.
- **Adaptability:** The architecture of TrID is inherently flexible, allowing them to be adapted for a broad range of applications. This adaptability stems from the ability to process inputs of varying lengths and the ease of integrating additional information.
- **Computational Efficiency:** The potential for omitting the decoder in Transformers, along with the parallelization capabilities of Transformers, can lead to significant reductions in training time and computational complexity. This also paves the way for batch processing of signals, contributing to real-time performance in practical applications.

VI. COMPARISON WITH TRADITIONAL APPROACH

In this section, we provide a comparison between our proposed GenAI-based models (TrID and VAE), and the traditional ED detector using only data in the time-domain.

A. GENERATION OF COMPARATIVE DATASETS

First, we examine the performance of the models in detecting the received LEO interference signals when its signal bandwidth: 1) 100% overlapped with GSO bandwidth, 2) 75% overlapped with GSO bandwidth, 3) 50% overlapped with GSO bandwidth and 4) 25% overlapped with GSO bandwidth. In other words, where the adjustment factor $B_{\text{adj},k}$ in (3) is 1, 0.75, 0.5 and 0.25 respectively. Therefore, to perform this comparison, we need to generate four new datasets, each referred to as the OVRLP% set representing the percentage of overlap within the data.

To generate these four OVRLP% sets, we considered only one LEO satellite pass ($k = \mathcal{K} = 1$). The simulation period is selected by experimental methods, where the LEO satellite is always visible to the GGS. The percentage of overlap between the GSO and LEO bandwidths is controlled by setting the GSO and LEO bandwidths at 50 MHz each and then adjusting the overlap bandwidth $B_{\text{overlap},k}$ in (3) according to the value that satisfies the target percentage, which will also require the change in the LEO carrier frequency $f_{c,k}$. The following steps outline the process of generating a single OVRLP% set:

- Initially, we fix GSO ModCod to QPSK, and the CNR values are selected within the range defined in Table 4 for the corresponding ModCod.
- The simulation runs with a single LEO satellite pass, "STARLINK-6173", starting at "01-Aug-2023 06:07:00", and a duration of $\mathcal{T} = 120$ seconds, and it samples LEO coordination and INR value every $\Delta\tau = 5$ ms, resulting in a total of $N = 2400$ samples from CNR and INR samples.
- We then repeat the simulation for other GSO ModCods listed in Table 4, i.e., 8PSK and 16APSK. This results in a total of three simulation rounds and a total of $N = 7200$ samples from CNR and INR values.
- Using simulation samples, we generate $N \times M_t$ time-domain interference data from (16). All N rows are then labeled as "1". In addition to the label, we also append the corresponding GSO ModCod scheme, the INR value, and off-axis angle to each row. This step forms the interference segment of 7200 data points to OVRLP% set.
- We also create interference-free data in the time-domain $N \times M_t$, from the magnitude of (14a), resulting in additional data points to the overall OVRLP% set. These data points are then labeled "0" and append the corresponding GSO ModCod, and two empty data columns to align with the other segment dimensions. This step forms the interference-free segment of 7200 data points to OVRLP% set.
- Finally, both segments are joined to form the full OVRLP% set, amounting in a total of $N = 14400$ time-domain data points and labels (i.e., $7200 \times M_t + 4$ interference-free data and $7200 \times M_t + 4$ interference data).

Four distinct OVRLP% sets are generated, each based on the varying degrees of overlap bandwidth B_{overlap}. By referring to equation (3), and with both B_x and B_i fixed to 50 MHz, the sets are created as follows:

1) OVRLP100 set: Featuring 100% overlapping percentage ($B_{\text{overlap}} = 50$ MHz, $f_{c,\text{leo}} = 11.750$ GHz)
2) OVRLP75 set: With 75% overlapping percentage ($B_{\text{overlap}} = 37.5$ MHz, $f_{c,\text{leo}} = 11.7625$ GHz)
3) OVRLP50 set: Comprising 50% overlapping percentage ($B_{\text{overlap}} = 25$ MHz, $f_{c,\text{leo}} = 11.775$ GHz)
4) OVRLP25 set: Including the 25% overlapping percentage ($B_{\text{overlap}} = 12.5$ MHz, $f_{c,\text{leo}} = 11.7875$ GHz).

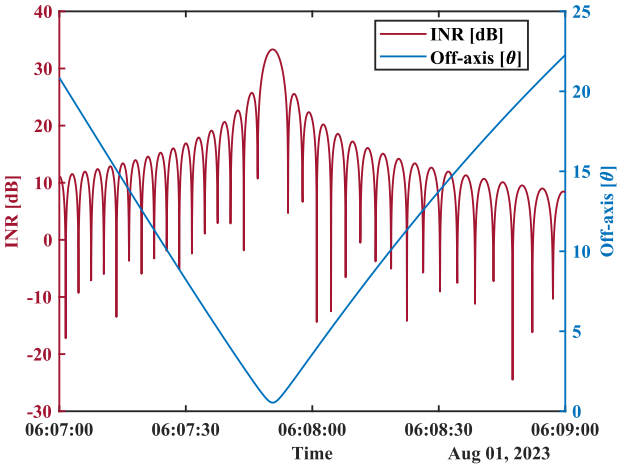

FIGURE 14. **LEO pass vs INR and off-axis angles.**

Fig. 14 showcases an example of the LEO off-axis angles and INR values during single simulation round, particularly the GSO at QPSK within the OVRLP100 set.

B. ENERGY DETECTOR APPROACH

An ED [43], is the optimal likelihood-ratio test for stochastic signals in white Gaussian noise (WGN) environments according to the classical detection theory [16]. ED is a fundamental tool for identifying the presence of interference signals in designated frequency bands. It functions by quantifying the energy content of received signal samples within a defined temporal window and comparing this value with a pre-established energy threshold. This mechanism enables the detector to effectively discern between GSO signals and scenarios encompassing both GSO and LEO signals.

Regarding the generated data, we know that the n^{th} data within N data points is a vector $y_n \rightarrow y_n^{\mathcal{A}}$ of length M_t, and each vector contains the magnitude values of the corresponding received signal. Hence, the energy (magnitude squared) E_n of each data y_n is calculated by squaring the amplitude of its samples and summing them up.

$$E_n = \sum_{m=1}^{M_t} y_n^2[m] \tag{40}$$

where $y_n[m]$ is the amplitude of the m^{th} sample in the signal y_n. An energy threshold β_E is set to determine whether a signal y_n contains an interference signal or not. This threshold is fixed and its value is derived from the Testing Set based on the optimal AUC Score approach as for the threshold of the ML models explained in Section V-B.2. In his case $\beta_E = 86.03$. The performance of the interference detector can be evaluated using the previously described interference detection performance metrics as in Table 5 and Table 6.

C. COMPARISON RESULTS

1) COMPARE FOR DIFFERENCE OVERLAPPING FACTOR

First, we compare the performance of TrID, VAE and ED using the aforementioned OVRLP% sets. Table 7 presents a

TABLE 7. Performance comparison of models across bandwidth overlap.

Overlap (%)	Model	Accuracy	TPR	FPR	F1 Score	AUC
100%	TrID	**0.8541**	**0.7867**	0.0785	**0.8435**	**0.8541**
	VAE	0.8442	0.7185	**0.0274**	0.8213	0.8442
	ED	0.8007	0.6754	0.0740	0.7721	0.8007
75%	TrID	**0.8431**	**0.7685**	0.0822	**0.8305**	**0.8431**
	VAE	0.8017	0.6369	**0.0336**	0.7626	0.8017
	ED	0.7578	0.5951	0.0794	0.7108	0.7578
50%	TrID	**0.8327**	**0.7571**	0.0812	**0.8227**	**0.8379**
	VAE	0.7526	0.5388	**0.0336**	0.6853	0.7526
	ED	0.7096	0.4999	0.0807	0.6325	0.7096
25%	TrID	**0.7936**	**0.6683**	0.0811	**0.7641**	**0.7936**
	VAE	0.6747	0.3817	**0.0324**	0.5398	0.6746
	ED	0.6378	0.3560	0.0786	0.4962	0.6387

comparative analysis of the three different models to detect NGSO-GSO interference in a time-domain representation of the signal y_n with varying degrees of bandwidth overlap between the NGSO and GSO signals.

In Table 7, TrID consistently outperforms the other models in all levels of bandwidth overlap. Its robustness to changes in overlap scenarios makes it a versatile model for different signal environments. VAE tends to minimize false alarms effectively, but struggles more than TrID with decreasing overlap in terms of accurately identifying interference. ED shows that traditional methods are less effective than the proposed GenAI-based approaches, especially as bandwidth overlap decreases, which likely introduces more complexity into the signal to which ED methods are not equipped to handle.

As a conclusion, in satellite communication systems, when choosing a model for interference detection across various environments constrains and possibilities of bandwidth overlaps, TrID may stand out as the most robust and high-performing model. Although VAE has merits, particularly in environments where false alarms are highly undesirable, its performance drops with reduced overlap make it less reliable than TrID in diverse conditions. Traditional ED is significantly outclassed by the GenAI-based models, highlighting the potential benefits of GenAI-based in signal processing tasks.

2) OTHER COMPARISONS

Based on the previous comparison, the models are more likely to detect interference in a fully overlap bandwidth scenarios than other scenarios. Therefore, we will focus on this next analysis only using the OVRLP100 set. In this section, we particularly investigate the impact of off-axis angles and INR values versus different GSO modulation schemes detection capabilities. The interference segment can be divided into three sub-segments based on GSO modulation schemes: [QPSK sub-segment, 8PSK sub-segment, and 16APSK sub-segment], each sub-segment contains 2400 data, and while different in GSO CNR values, each sub-segment contain the same LEO off-axis angles and the corresponding CNR values as in Fig. 14. The GSO CNR values range from 2.4 to 6.6 dB in the QPSK sub-segment, 6.7 to 9 dB for 8PSK, and 9.1 to 14 for 16APSK. The probability of detection P_D (or TPR) values are tested using coherent chunks of fixed sizes from each the sub-segments after sorted it out depending on the parameter of interest using the TrID, VAE, and ED.

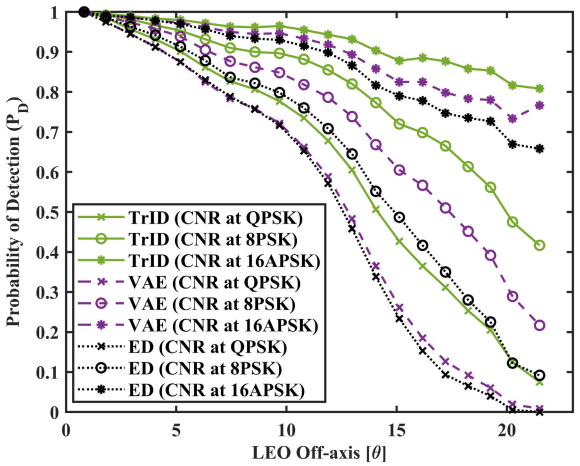

FIGURE 15. Detection vs LEO off-axis Angles for Various GSO ModCods.

The ability to maintain high interference detection performance across a range of off-axis angles is particularly important for systems that involve moving satellites, such as those in NGSO. We are comparing the models detection performance based on the LEO off-axis angles as seen from GGS. A small off-axis angle corresponds to a higher receive GSO ground station gain, therefore increasing the probability of detection. The previous hypothesis is validated with the results shown in Fig. 15, where the probability of detection is plotted with respect to the LEO link off-axis angle.

Based on the results in Fig. 15, we observed the following

- **Off-axis Angle Consideration**: When examining the probability detection with respect to the LEO off-axis angle, all models demonstrate a decreasing trend in P_D as the off-axis angle increases. This trend is expected because larger off-axis angles typically result in a weaker signal and more difficult detection. Thus, the models are more likely to detect LEO interference signals when their off-axis angles are close to the in-line interference scenario (i.e., LEO off-axis angle $\approx$ GSO boresight angle $\theta_0 = 0°$).
- **Impact of GSO Modulation Schemes**: All models perform best in the 16APSK GSO modulation scheme, and the performance decreases as the GSO modulation scheme decreases in complexity. For the lower modulation scheme (i.e., GSO in QPSK), the models detection probability decreases to zero for LEO off-axis angles higher than 20° with TrID capturing interference in slightly higher angles. For GSO scenarios in 8PSK and 16APSK, TrID maintains its detection capability at superior performance compared to VAE and ED as well. We noticed that the model performance in detecting relatively higher off-axis angles (i.e., higher than 20°) increases for higher GSO modulation schemes.

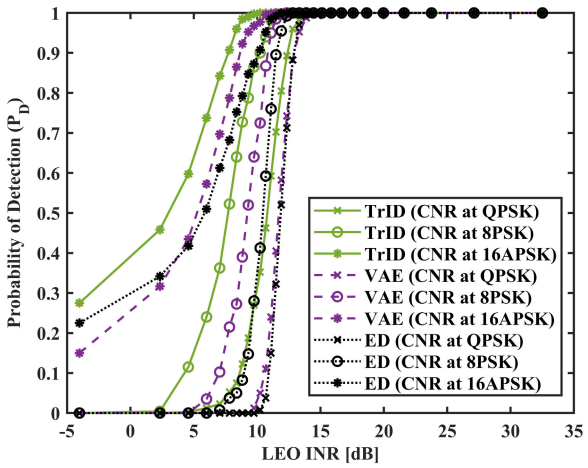

FIGURE 16. Detection vs LEO INR Values for various GSO ModCods.

- **TrID Performance**: TrID maintains the highest P_D over a larger range of off-axis angles, reinforcing its robustness. VAE and ED show a steeper decline in performance, with the ED being the most affected. This suggests that the TrID is better equipped to detect LEO interfering signals when they are not perfectly aligned with the GSO. Moreover, for different GSO modulation schemes data, TrID maintains a superior P_D across all modulation schemes compared to other models.
- **VAE Performance**: VAE detection performance also decreases with increasing off-axis angles, but at a faster rate than the TrID. This indicates that the VAE is somewhat sensitive to LEO off-axis angle, which could limit its effectiveness in operational environments where LEO usually does not perfectly align with GSO.
- **ED Performance**: The performance of the ED shows the most significant decline with increasing off-axis angles. This steep performance drop highlights the ED vulnerability to low levels of interference. The ED performance gap drops more significantly with higher-order modulations (i.e., 16APSK).

Although the INR values are depending on LEO receiving off-axis angles at GGS, lower angles do not always lead to high INR, this due to the side lobes and nulls of the GGS beam pattern, as can be seen in Fig. 14. Higher INR values can provide a more distinct separation between the GSO desired signal and LEO interfering signals, which shall be exploited by the proposed models shall exploit to improve the detection performance. Fig. 16 shows the evolution of the probability of detection versus the INR values observed at the GSO ground station.

Based on the results in Fig. 16, we observe the following

- **INR values Consideration**: All models' performance increases with higher INR values, they are capable of detecting LEO interference signals with INR value around 15 dB and higher. The ability of the TrID model to maintain high detection performance across a range of INR values is essential for practical applications, as it ensures reliability in various interference conditions.
- **Impact of GSO Modulation Schemes**: The model performance in detecting relatively small INR values increases for higher GSO modulation schemes. The models can still detect up to -5 dB INR values at the 16APSK sub-segment, 5 dB INR values at the 8PSK sub-segment, with TrID standing out across all the modulation schemes sub-segments and ED being the worse.
- **TrID Performance**: TrID consistently outperforms both VAE and ED across all GSO modulation schemes with respect to LEO INR values. Its performance is particularly notable at lower INR values, this implies that the TrID is more highly capable of distinguishing between the desired GSO signal and LEO interfering signals when the interference is within the noise level.
- **VAE Performance**: The VAE shows moderate detection performance, which is generally less than that of the TrID but superior to that of the ED. Its performance also degrades more gracefully compared to the ED as INR decreases, which can be advantageous in lower-quality signal environments. The VAE model also shows improved detection accuracy as INR increases, but to a lesser extent compared to the TrID.
- **ED Performance**: ED performance is less competitive compared to GenAI-based models, particularly at lower INR values. However, it shows a gradual increase in P_D with increasing INR, suggesting that it can still be somewhat effective in high interference scenarios.

TrID emerges as the superior model due to its high interference detection performance in comparison to other models, and it is also less sensitive to the complexity of the modulation scheme, making it a versatile and reliable choice for detecting NGSO to GSO interference. The VAE could serve as a fallback due to its moderate performance, while the ED could be considered for scenarios where computational simplicity is more critical than detection accuracy. Given these observations, the TrID is recommended as the best model for the task of NGSO to GSO interference detection due to its robustness to signal quality variations and its superior performance in both off-axis angles and INR values scenarios.

VII. CONCLUSION

This paper addressed the problem of interference detection in satellite communication, where signals from NGSO satellites have the potential to disrupt communications with GSO satellites when operating in the same spectral bands. We employ realistic simulations of satellite positions and trajectories, using actual system parameters to create interference scenarios. We proposed and evaluated different ML performance for the interference detection task. The proposed ML models are adeptly trained to discern interference in both the time and frequency domains of the received signals. The core contribution of this work is the development of GenAI-based models (TrID, and VAE) interference detectors designed to

identify LEO interference by generating new samples of the original GSO signals.

The findings reveal that the models exhibits higher accuracy for detecting interference in the time-domain signal representations compared to the frequency-domain representations, with TrID being superior compared to VAE and other ML models. Moreover, TrID, VAE and ED were put in a comparison to explore the impact of varying GSO modulation schemes, bandwidth overlapping scenarios, LEO off-axis angles, and the interference power values (INR) on the detection accuracy, where TrID consistently outperforms both the VAE and ED across all the scenarios. Our research provides actionable insights for satellite communication operators. By understanding the efficacy of GenAI-based models in interference detection, they can make informed decisions and trade-off about integrating these technologies into existing and future satellite communication infrastructures.

Future work should focus on enhancing the models' capabilities in the frequency domain, potentially exploring hybrid models or advanced feature engineering techniques. Multiple models could be trained to detect interference in a single modulation scheme each, instead of training the models in all modulation schemes at once and see if that makes a difference. The data used in this paper will be publicly available on the Smart-Space project website [32].

REFERENCES

[1] H. Al-Hraishawi, H. Chougrani, S. Kisseleff, E. Lagunas, and S. Chatzinotas, "A survey on nongeostationary satellite systems: The communication perspective," *IEEE Commun. Surveys Tuts.*, vol. 25, no. 1, pp. 101–132, 1st Quart., 2023.

[2] M. Jalali, F. Ortiz, E. Lagunas, S. Kisseleff, L. Emiliani, and S. Chatzinotas, "Joint power and tilt control in satellite constellation for NGSO-GSO interference mitigation," *IEEE Open J. Veh. Technol.*, vol. 4, pp. 545–557, 2023.

[3] *Radio Regulations*, ITU, Geneva, Switzerland, 2020.

[4] ITU. *ITU Member States Agree on New Global Treaty to Advance Digital Transformation*. Accessed: Dec. 31, 2023. [Online]. Available: https://www.itu.int/en/mediacentre/Pages/PR-2023-12-15-WRC23-closing-ceremony.aspx

[5] C. Wang, D. Bian, S. Shi, J. Xu, and G. Zhang, "A novel cognitive satellite network with GEO and LEO broadband systems in the downlink case," *IEEE Access*, vol. 6, pp. 25987–26000, 2018.

[6] M. Jalali, F. G. Ortiz-Gomez, E. Lagunas, S. Kisseleff, L. Emiliani, and S. Chatzinotas, "Radio regulation compliance of NGSO constellations' interference towards GSO ground stations," in *Proc. IEEE 33rd Annu. Int. Symp. Pers., Indoor Mobile Radio Commun. (PIMRC)*, Sep. 2022, pp. 1425–1430.

[7] C. Politis, S. Maleki, C. Tsinos, S. Chatzinotas, and B. Ottersten, "On-board the satellite interference detection with imperfect signal cancellation," in *Proc. IEEE 17th Int. Workshop Signal Process. Adv. Wireless Commun. (SPAWC)*, Jul. 2016, pp. 1–5.

[8] L. Xie, Y. Zhuang, X. Zhuang, and X. Zeng, "Satellite interference signal classification using improved MLP model," in *Proc. IEEE Int. Conf. Unmanned Syst. (ICUS)*, Oct. 2022, pp. 635–640.

[9] C. Hao, D. Feng, Q. Zhang, and X.-G. Xia, "Interference geolocation in satellite communications systems: An overview," *IEEE Veh. Technol. Mag.*, vol. 16, no. 1, pp. 66–74, Mar. 2021.

[10] D. Peng, D. He, Y. Li, and Z. Wang, "Integrating terrestrial and satellite multibeam systems toward 6G: Techniques and challenges for interference mitigation," *IEEE Wireless Commun.*, vol. 29, no. 1, pp. 24–31, Feb. 2022.

[11] A. U. Makarfi and K. A. Hamdi, "Interference analysis of energy detection for spectrum sensing," *IEEE Trans. Veh. Technol.*, vol. 62, no. 6, pp. 2570–2578, Jul. 2013.

[12] M. N. Vázquez et al., "Machine learning for satellite communications operations," *IEEE Commun. Mag.*, vol. 59, no. 2, pp. 22–27, Feb. 2021.

[13] I. Goodfellow et al., "Generative adversarial nets," in *Proc. Adv. Neural Inf. Process. Syst.*, vol. 27, Dec. 2014, pp. 2672–2680.

[14] D. P. Kingma and M. Welling, "Auto-encoding variational Bayes," 2013, *arXiv:1312.6114*.

[15] A. Vaswani et al., "Attention is all you need," in *Proc. Adv. Neural Inf. Process. Syst.*, 2023, pp. 1–11.

[16] S. Kay, *Fundamentals of Statistical Signal Processing: Detection Theory*. Upper Saddle River, NJ, USA: Prentice-Hall, 1998.

[17] J. Font-Segura, G. Vazquez, and J. Riba, "Nonuniform sampling walls in wideband signal detection," *IEEE Trans. Signal Process.*, vol. 62, no. 1, pp. 44–55, Jan. 2014.

[18] M. V. Lipski, S. Kompella, and R. M. Narayanan, "Practical implementation of adaptive threshold energy detection using software defined radio," *IEEE Trans. Aerosp. Electron. Syst.*, vol. 57, no. 2, pp. 1227–1241, Apr. 2021.

[19] ETSI, *Second Generation Framing Structure, Channel Coding and Modulation Systems for Broadcasting, Interactive Services, News Gathering and Other Broadband Satellite Applications Part II: S2-Extensions (DVBS2X)*, Standard ETSI: EN 302 307-2, Digit. video Broadcast. (DVB), 2014, pp. 13–24.

[20] F. Dimc, G. Baldini, and S. Kandeepan, "Experimental detection of mobile satellite transmissions with cyclostationary features," *Int. J. Satell. Commun. Netw.*, vol. 33, no. 2, pp. 163–183, Mar. 2015.

[21] F. Fourati and M.-S. Alouini, "Artificial intelligence for satellite communication: A review," *Intell. Converg. Netw.*, vol. 2, no. 3, pp. 213–243, 2021.

[22] F. Ortiz et al., "Onboard processing in satellite communications using AI accelerators," *Aerospace*, vol. 10, no. 2, p. 101, Jan. 2023.

[23] G. Fontanesi et al., "Artificial intelligence for satellite communication and non-terrestrial networks: A survey," 2023, *arXiv:2304.13008*.

[24] L. Pellaco, N. Singh, and J. Jaldén, "Spectrum prediction and interference detection for satellite communications," in *Proc. 37th Int. Commun. Satell. Syst. Conf. (ICSSC)*, Okinawa, Japan, 2019, pp. 1–18, doi: 10.1049/cp.2019.1269.

[25] A. Saifaldawla, F. G. Ortiz-Gomez, E. Lagunas, S. Daoud, and S. Chatzinotas, "NGSO-to-GSO satellite interference detection based on autoencoder," in *Proc. IEEE 34th Annu. Int. Symp. Pers., Indoor Mobile Radio Commun. (PIMRC)*, Sep. 2023, pp. 1–7.

[26] J. D. Kraus and R. J. Marhefka, *Antennas for All Applications*. Cambridge, MA, USA: SAO/NASA Astrophysics Data System, 2002.

[27] G. N. Watson, *A Treatise on the Theory of Bessel Functions*, vol. 2. Farmgate, Dhaka: The Univ. Press, 1922.

[28] S. Daoud, G. Eappen, F. Ortiz, E. Lagunas, W. Martins, and S. Chatzinotas, "CNN-based on-board interference detection in satellite systems: An analysis of dataset impact on performance," in *Proc. IEEE Int. Conf. Acoust., Speech, Signal Process. Workshops (ICASSPW)*, Jun. 2023, pp. 1–5.

[29] P. Welch, "The use of fast Fourier transform for the estimation of power spectra: A method based on time averaging over short, modified periodograms," *IEEE Trans. Audio Electroacoustics*, vol. AU-15, no. 2, pp. 70–73, Jun. 1967.

[30] Mathworks Inc. *Interference From Satellite Constellation on Communications Link—MATLAB & Simulink—MathWorks Benelux*. Accessed: May 11, 2023. [Online]. Available: https://nl.mathworks.com/help/satcom/ug/interference-from-satellite-constellation-on-comms-link.html

[31] CelesTrak. *CelesTrak: Current GP Element Sets*. Accessed: Jul. 31, 2023. [Online]. Available: https://celestrak.org/NORAD/elements/

[32] E. Lagunas. *FNR SmartSpace Project: Leveraging AI to Empower the Next Generation of Satellite Communications*. Accessed: Apr. 29, 2024. [Online]. Available: https://fnr-smartspace-project.uni.lu/datasets/

[33] M. Sakurada and T. Yairi, "Anomaly detection using autoencoders with nonlinear dimensionality reduction," in *Proc. MLSDA 2nd Workshop Mach. Learn. Sensory Data Anal.*, New York, NY, USA, Dec. 2014, pp. 4–11.

[34] S. Kullback, *Information Theory and Statistics*. Chelmsford, MA, USA: Courier Corporation, 1997.

[35] A. Tharwat, "Classification assessment methods," *Appl. Comput. Informat.*, vol. 17, no. 1, pp. 168–192, Jul. 2020, doi: 10.1016/j.aci.2018.08.003.

[36] S. Schmidl, P. Wenig, and T. Papenbrock, "Anomaly detection in time series: A comprehensive evaluation," *Proc. VLDB Endow.*, vol. 15, no. 9, pp. 1779–1797, 2022.

[37] SES. *SES Network Map*. Accessed: May, 11, 2023. [Online]. Available: https://www.ses.com/sites/default/files/network_map/SES_Network Map_RGB_180827_Rise_BlueVersion-p.pdf
[38] ESA. *ESA—Satellite Frequency Bands*. Accessed: Jul. 31, 2023. [Online]. Available: https://www.esa.int/Applications/Connectivity_and_Secure_Communications/Satellite_frequency_bands
[39] W. Wiltshire, "Application for fixed satellite service by space exploration holdings, LLC," Federal Commun. Commission (FCC), Washington, DC, USA, Tech. Rep. SAT-LOA20200526-00055 and SAT-AMD-20210818-00105, Dec. 2020.
[40] B. D. Weimer, "Application for fixed satellite service by worldVu satellites limited, debtor-in-possession," Federal Commun. Commission (FCC), Washington, DC, USA, Tech. Rep. SAT-MPL-20200526-00062 and SATMPL2020052600062, Apr. 2023.
[41] ITU. *Allowable Short-Term Error Performance for a Satellite Hypothetical Reference Digital Path*. Accessed: Aug. 20, 2023. [Online]. Available: https://www.itu.int/dms_pubrec/itu-r/rec/s/R-REC-S.2099-0-201612-I!!PDF-E.pdf
[42] S. Varrette, H. Cartiaux, S. Peter, E. Kieffer, T. Valette, and A. Olloh, "Management of an academic HPC & research computing facility: The ULHPC experience 2.0," in *Proc. 6th ACM High Perform. Comput. Cluster Technol. Conf. (HPCCT)*. Fuzhou, China: Association for Computing Machinery (ACM), Jul. 2022, pp. 14–24.
[43] H. Urkowitz, "Energy detection of unknown deterministic signals," *Proc. IEEE*, vol. 55, no. 4, pp. 523–531, Apr. 1967.

ALMOATSSIMBILLAH SAIFALDAWLA (Graduate Student Member, IEEE) received the B.Sc. degree (Hons.) in electronics engineering technology from the University of Gezira (UofG), Sudan, in June 2018, and the M.Eng. degree in communication and information engineering from Chongqing University of Posts and Telecommunications (CQUPT), China, in June 2022. He is currently pursuing the Ph.D. degree in computer science and computer engineering with the SIGCOM Research Group, Interdisciplinary Centre for Security, Reliability and Trust (SnT), University of Luxembourg. His research interests include wireless communications, resource management, and machine learning for satellite communications.

FLOR ORTIZ (Member, IEEE) received the B.S. degree in telecommunications engineering and the M.S. degree in electrical engineering-telecommunications from the Universidad Nacional Autónoma de México (UNAM), Mexico City, Mexico, in 2015 and 2016, respectively, and the Ph.D. degree in telecommunication engineering from the Universidad Politecnica de Madrid (UPM), Madrid, Spain, in September 2021. During the Ph.D. degree, she performed a research period at the University of Bologna, Bologna, Italy. She started a close collaboration between UPM and the University of Bologna, opening a new research line for both groups on applying machine learning for radio resource management. She has joined as a Research Associate with the Interdisciplinary Centre for Security, Reliability, and Trust (SnT), University of Luxembourg. Her research interests include implementing cutting-edge machine learning techniques, including continual learning and neuromorphic computing for operations in satellite communications systems.

EVA LAGUNAS (Senior Member, IEEE) received the M.Sc. and Ph.D. degrees in telecommunications engineering from the Polytechnic University of Catalonia, Barcelona, Spain, in 2010 and 2014, respectively. From 2009 to 2013, she was a Research Assistant with the Department of Signal Theory and Communications, UPC. During the Summer of 2009, she was a Guest Research Assistant with the Department of Information Engineering, Pisa, Italy. From November 2011 to May 2012, she held a visiting research appointment with the Center for Advanced Communications, Villanova University, Villanova, PA, USA. In 2014, she joined the Interdisciplinary Centre for Security, Reliability and Trust (SnT), University of Luxembourg, where she is currently a Research Scientist. Her research interests include terrestrial and satellite system optimization, spectrum sharing, resource management, and machine learning.

ABUZAR B. M. ADAM (Member, IEEE) received the M.Eng. degree in computer science and technology from Xiamen University, Xiamen, China, in 2017, and the Ph.D. degree from Chongqing University of Posts and Telecommunications, Chongqing, China, in 2021. He was a Postdoctoral Fellow and a Lecturer with the School of Communications and Information Engineering. He was a Research Assistant Professor with the Institute of Next-Generation Networks, Chongqing University of Posts and Telecommunications. He is currently a Research Associate with the Interdisciplinary Centre for Security, Reliability and Trust (SnT), University of Luxembourg, Luxembourg. His research interests include AI-enabled wireless networks, RIS-assisted wireless networks, integrated terrestrial/non-terrestrial networks, convex optimization, and machine learning and applications. He was a recipient of the 2021 Outstanding Doctoral Student Award.

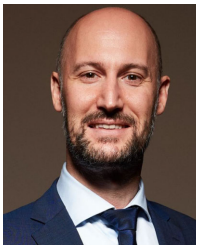

SYMEON CHATZINOTAS (Fellow, IEEE) received the M.Eng. degree in telecommunications from the Aristotle University of Thessaloniki, Greece, in 2003, and the M.Sc. and Ph.D. degrees in electronic engineering from the University of Surrey, U.K., in 2006 and 2009, respectively. He is currently a Full Professor/Chief Scientist I and the Head of the Research Group SIGCOM, Interdisciplinary Centre for Security, Reliability and Trust, University of Luxembourg. In parallel, he is an Adjunct Professor with the Department of Electronic Systems, Norwegian University of Science and Technology, and a Collaborating Scholar with the Institute of Informatics and Telecommunications, National Centre of Scientific Research "Demokritos." In the past, he was lectured as a Visiting Professor with the University of Parma, Italy, and contributed in numerous research and development projects for the Institute of Telematics and Informatics, Center of Research and Technology Hellas, and the Mobile Communications Research Group, Center of Communication Systems Research, University of Surrey. He has authored more than 700 technical papers in refereed international journals, conferences, and scientific books, and has received numerous awards and recognitions, including the IEEE Fellowship and the IEEE Distinguished Contributions Award. He is also on the Editorial Board of IEEE TRANSACTIONS ON COMMUNICATIONS, IEEE OPEN JOURNAL OF VEHICULAR TECHNOLOGY, and the *International Journal of Satellite Communications and Networking*.